Journal of Magnetic Resonance 213 (2011) 32–45

Contents lists available at SciVerse ScienceDirect

Journal of Magnetic Resonance

journal homepage: www.elsevier.com/locate/jmr

Investigating the intermediates in the reaction of ribonucleoside triphosphate reductase from *Lactobacillus leichmannii*: An application of HF EPR–RFQ technology

Julia Manzerova, Vladimir Krymov, Gary J. Gerfen *

Department of Physiology and Biophysics, Albert Einstein College of Medicine, 1300 Morris Park Ave., Bronx, NY 10461, United States

ARTICLE INFO

Article history:
Received 18 August 2011
Available online 31 August 2011

Keywords:
Electron paramagnetic resonance (EPR)
High-frequency (HF)
Rapid freeze-quench (RFQ)
Ribonucleotide reductase
Ribonucleoside triphosphate reductase (RTPR)
Lactobacillus leichmannii
Exchange interaction (J_{ex})
Dipolar interaction
Enzyme
Active site
Adenosylcobalamin
Thiyl radical
Homolysis
Exchange-coupled pair
Enzyme
Enzymology

ABSTRACT

In this investigation high-frequency electron paramagnetic resonance spectroscopy (HFEPR) in conjunction with innovative rapid freeze-quench (RFQ) technology is employed to study the exchange-coupled thiyl radical–cob(II)alamin system in ribonucleotide reductase from a prokaryote *Lactobacillus leichmannii*. The size of the exchange coupling (J_{ex}) and the values of the thiyl radical *g* tensor are refined, while confirming the previously determined (Gerfen et al. (1996) [20]) distance between the paramagnets. Conclusions relevant to ribonucleotide reductase catalysis and the architecture of the active site are presented. A key part of this work has been the development of a unique RFQ apparatus for the preparation of millisecond quench time RFQ samples which can be packed into small (0.5 mm ID) sample tubes used for CW and pulsed HFEPR – lack of this ability has heretofore precluded such studies. The technology is compatible with a broad range of spectroscopic techniques and can be readily adopted by other laboratories.

1. Introduction

Ribonucleotide reductases (RNRs) are present in all cellular non-parasitic organisms characterized so far, and are also encoded by many DNA viruses [1–5]. These enzymes catalyze the reduction of purine and pyrimidine nucleotides to the corresponding deoxyribonucleotides (dNTPs), the only known means of de novo generating precursors for both DNA replication and repair. RNRs across different species share key functional features. First, they use a cysteine-based thiyl radical located in the active site to initiate the chain of substrate-based events that culminate in the final product, a dNTP. Second, to maintain a balanced supply of dNTPs, all RNRs are allosterically regulated by the final product. Binding of a dNTP at a specificity site distinct from the catalytic site shifts the conformational equilibrium of the enzyme towards the state favoring reduction of the nucleotide that is in short supply at the time [6,7]. Similarity in the catalytic and regulatory strategies employed by the enzymes is reflected in the striking conservation of the active site folding topology, general architecture of catalytic subdomains and arrangement of the key catalytic elements: this is despite the low overall sequence identity between different reductases [3,8].

Based on the type of metallocofactor used to generate the thiyl radical, ribonucleotide reductases are divided into three broad classes [2,3,9–12]. A representative reductase from class II, the ribonucleotide triphosphate reductase from a prokaryote *Lactobacillus leichmanii* (RTPR), possesses qualities that have made it a paradigm of reductases and especially attractive for research. First, it is a relatively small (82 kDa) monomeric protein, and yet it preserves the major catalytic features of its multimeric congeners, including the general fold of the catalytic domains and the allosteric regulation by dNTPs. The overall reaction mechanism, including the initiation of the substrate-based events by a thiyl radical, is the same as in the other RNRs. Scheme 1 summarizes the generally accepted steps in the mechanism. Upon binding allosteric effector, the carbon–cobalt bond of the adenosylcobalamin cofactor is homolytically cleaved, producing cob(II)alamin and an adenosyl radical (B), which rapidly abstracts a hydrogen atom from a conserved top-face cysteine. Species C is the exchange coupled

* Corresponding author. Fax: +1 718 430 8819.
E-mail address: gary.gerfen@einstein.yu.edu (G.J. Gerfen).

1090-7807/$ - see front matter © 2011 Elsevier Inc. All rights reserved.
doi:10.1016/j.jmr.2011.08.030

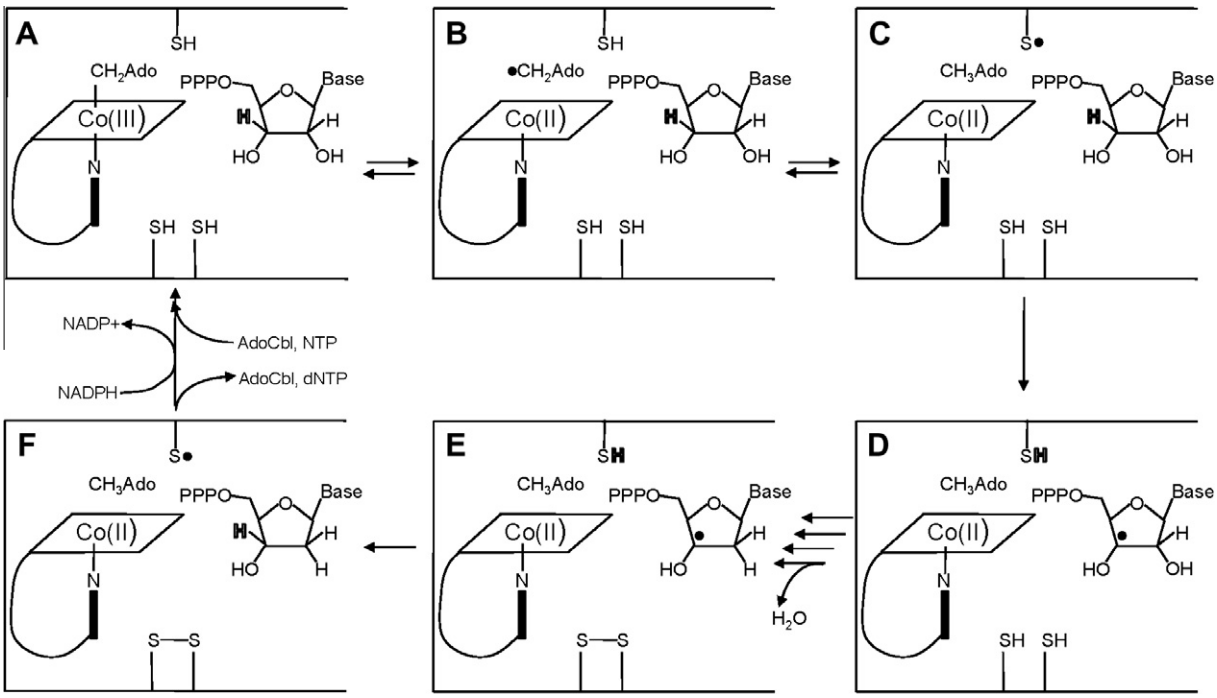

Scheme 1. Generalized proposed reaction scheme for ribonucleotide reductases.

cob(II)alamin–thiyl radical pair, which is the subject of this study. The thiyl radical extracts the 3′ hydrogen from ribonucleotide substrate to form a substrate-based radical species. Several steps occur at this stage, resulting in formation of disulfide bridge between two bottom-face conserved cysteines and the loss of water. The final deoxyribonucleotide product is formed when the same hydrogen atom is transferred from the cysteine to the 3′ position. Release of product and cofactor, reduction of the enzyme, and binding of new substrate and cofactor return the system to the initial state. Because these steps following the generation of the thiyl radical are thought to be common across the enzyme classes, experimental results obtained with RTPR as a model can be extrapolated to most RNRs. The results are relatively uncomplicated in interpretation because RTPR has only one active site and one allosteric effector binding site. Second, RTPR uses adenosylcobalamin (AdoCbl) as a cofactor, and is capable of activating the C–Co bond even in the absence of substrate – as long as the allosteric effector is present. Thus, in the absence of substrate, RTPR has been shown to generate a catalytically relevant intermediate in a kinetically competent fashion [13–21]. These characteristics of RTPR make it an ideal representative of RNRs to study the mechanism of ribonucleotide reduction and inactivation [22–24], as well as the mechanism through which AdoCbl-containing enzymes enhance the rate of the carbon–cobalt bond homolysis by at least 10 orders of magnitude compared that of nonenzymatic thermolysis [25].

Given the paramagnetic nature of the intermediates involved at all stages of the RTPR reaction, and the millisecond time regime when these intermediates accumulate, RTPR research has significantly benefited from X-band EPR combined with the technique of Rapid Freeze Quench (RFQ). When a mixture of pre-reduced RTPR, AdoCbl and an allosteric effector (such as dGTP) is incubated for 50–200 ms and then freeze-quenched, an interesting EPR signal develops [16] with the kinetics that closely parallel spectrophotometrically detected evolution of a Co(II) species [15,26], which was recognized as an intermediate in the ribonucleotide reduction reaction. The effective g value spectral crossing point (2.12) and Co(II) nuclear hyperfine coupling (50 G) of this signal differ from those of nonenzymatically produced cob(II)alamin bound to the enzyme (2.23 and 110 G, respectively [21,27]). To assign the identity of this intermediate, two-frequency RFQ/EPR experiments on deuterated enzyme were combined with computer simulations [20]. This work unambiguously demonstrated that AdoCbl in RTPR does not abstract a hydrogen atom from the substrate, as previously thought, but rather serves to generate the thiyl radical on a specific active site cysteine (C408). Co(II) is coupled to the cysteine via dipolar and exchange interactions, and the computer analysis of these parameters revealed the distance between paramagnets to be on the order of 6.5 Å, and the angle between the interspin vector and the corrin ring normal of about 60° [20].

X-band EPR, however, often lacks the resolving power to extract the full scope of the information contained in a biological sample. The frozen solution EPR linewidth at X-band is often dominated by hyperfine interactions, and g-value anisotropy and/or overlapping signal from distinct paramagnetic species whose g tensors have similar values may remain unresolved [28–30]. It is therefore imperative to conduct high-frequency (greater than 95 GHz) and multi-frequency EPR studies. In recent years, EPR has seen an explosion of interest in the high-frequency (HF) regime, and HF finds use in most contemporary state-of-the-art EPR experiments [31–34]. A system of two unpaired electrons a and b and a nucleus with a nonzero spin angular momentum I coupled to the electron a, in an external magnetic field B is described by the Hamiltonian

$$\widehat{H} = \beta_e B \cdot g_a \cdot \widehat{S}_a + \beta_e B \cdot g_b \cdot \widehat{S}_b - \beta_n g_n B \cdot \widehat{I} + \widehat{S}_a \cdot A \cdot \widehat{I} + 2\widehat{S}_a \cdot D \cdot \widehat{S}_b - J_{ex}\widehat{S}_a \cdot \widehat{S}_b \quad (1)$$

where β_e is Bohr magneton, g_a and g_b are the g values of the two electrons, S_a and S_b are the electron spin operators, D is the zero-field splitting tensor, J_{ex} is the isotropic exchange coupling constant. At higher fields, the frequency-dependent terms of the spin Hamiltonian (electron Zeeman and nuclear Zeeman interactions: first, second and third terms in the Eq. (1); the nuclear Zeeman interaction becomes significant in double resonance experiments) are separated from the spin-independent terms (hyperfine, exchange and dipole–dipole interactions: the last three terms in the Eq. (1)). Selective excitation of molecular orientations also becomes possi-

ble. As a result, peaks corresponding to individual *g* values are spectrally separated, and components of individual *g* tensors, as well as contributions from different species, become resolved. In addition, HF EPR allows determination of the zero-field splitting (ZFS) parameters for $S > 1/2$ spin systems, where the zero-field splitting energies may be greater than the X-band excitation quantum [33,35,36]. Our laboratory is equipped with a home-built HF (D-band, 130 GHz) spectrometer with continuous-wave (CW), pulsed and ENDOR capabilities. To take advantage of this instrument for the study of enzymatic reactions such as the one catalyzed by RTPR, it is necessary to prepare rapid-freeze samples in the millisecond time regime. However, the shorter wavelength of the D-band radiation (2 mm, as opposed to 3 cm characteristic of X-band) dictates the use of correspondingly small resonators and sample holder tubes. The internal diameter of the quartz tubes suitable for the D-band EPR spectrometer is $\leqslant$0.5 mm. This reduction in dimensions limits the utility of the conventional RFQ that relies on a liquid cryogen for terminating the reaction, as discussed below.

In the RFQ experiment, as first developed by Bray and co-workers [37–39] and subsequently improved upon [40,41], the reaction components are ejected from two syringes coupled through delivery tubing to a mixing chamber. The reaction is initiated in this chamber and the mixture exits through a common aging tube whose length, together with the volumetric velocity of the solution, determines the age of the reaction when it reaches the outlet. The reaction is arrested on impact with a bath of isopentane (or another cryogenic liquid with a boiling point below that of the impacting solution) kept at 130–135 K (Fig. 1). The slurry of particles in isopentane is then collected and packed into the EPR tubes for further study. Packing of isopentane slurry into the small tubes is impractical for a number of reasons: drawing the liquid cryogen into the sample tubes is problematic [42] since the sample ends up being heavily diluted; when sample particles are sufficiently small (a requirement for efficient freeze-quenching and temporal homogeneity of the sample) they acquire electrostatic charge [42–44] and are repelled from each other, escaping the bore of the tube; in addition, the sample tubes become covered with isopentane on the outside. Isopentane solidifies at 113 K, above the 77 K or 4 K commonly used for EPR of frozen samples. Since the temperature of the primary coolant (liquid nitrogen) is fixed at 77 K, that of isopentane bath must be vigilantly monitored to prevent its solidification, and liquid nitrogen quickly added and decanted in response to fluctuations in the temperature of isopentane. A heated metal rod is sometimes kept on hand for emergency warming. Even with larger EPR tubes, the film of solid isopentane increases the external diameter of the sample tube, complicating the process of sample tube loading into and extraction from the EPR probe.

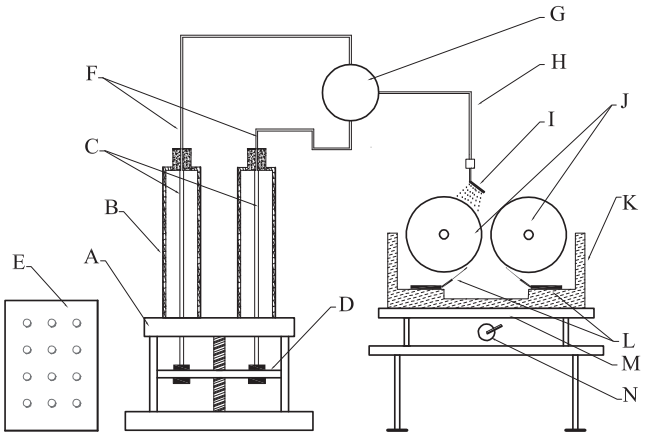

Fig. 1. Block diagram of the rapid freeze-quench apparatus. (A) Syringe mounting plate, (B) syringe holders, (C) plungers, (D) ram, (E) pulse programming unit, (F) reagent delivery hoses, (G) mixer, (H) aging hose, (I) nozzle, (J) wheels, (K) quenching basin (*here shown in cross-section*), (L) scrapers and scraper holders, (M) movable platform for the quenching basin, (N) handle for adjusting the platform height.

The simplest attempt to remedy the problem involved slowing down the velocity of the jet (to 20–30 m s^{-1}) [38,44], but undoubtedly this approach led to the diminished the quality of the sample. Spraying into cold ethane (melting point −181.76° C (89.34 K), boiling point −89° C (184 K)) and then letting ethane evaporate while the sample tube is kept in cold isopentane [45] was another method of collecting the sample. Other workers suctioned off isopentane from the sample compartment through a porous disk [42]; centrifuged the isopentane/sample slurry to obtain sample that could be packed into sample tubes [46]. Despite these efforts, to our knowledge there are no published accounts of packing liquid cryogen-quenched samples into small sample tubes, such as those used for D-band EPR (quartz, ID = 0.5 mm, OD = 0.7 mm).

To overcome these limitations, we have developed a freeze-quench apparatus that utilizes turbulent flow through a T-shaped mixer and cold-block freezing technology to uniformly and reliably stop reactions of biological interest after variable millisecond delays. Cold-block freezing originated in the efforts by electron microscopists to withdraw heat from biological specimens rapidly enough to achieve vitrification and prevent formation of the damaging ice crystals [47–50]. It involves bringing the sample into rapid contact with a metal (copper, brass, aluminum, silver) surface that had been cooled by liquid nitrogen or liquid helium. This method takes advantage of superior thermal conductivity of metals compared to that of liquid cryogens (thermal conductivity of crude copper at 77 K is 460 J m^{-1} s^{-1} K^{-1}, thermal conductivity of isopentane at its freezing point of 113 K is 0.1 J m^{-1} s^{-1} K^{-1}) and large heat capacity, which increases with decreasing temperature. As an additional benefit, metals do not develop the insulating boiling film due to the *Leidenfrost effect* [51,52] and the experimenter can control the area of contact between the specimen and the cooling surface.

The described RFQ apparatus accomplishes rapid freeze-quenching by spraying a fine mist of the reaction mixture on copper wheels that are kept at 77 K (cooled by liquid nitrogen). Packing the resulting sample "snow" suspended in liquid nitrogen into the small D-band tubes is easily accomplished. This RFQ apparatus in combination with D-band (130 GHz) EPR spectroscopy is used to investigate the exchange-coupled cobalamin-thiyl radical intermediate generated on the millisecond time scale in RTPR. The higher magnetic field (4 T vs. 0.3 T at X-band) allows the reevaluation of the thiyl radical *g*-values and the electron–electron exchange interaction, and gives insight into the structure of the active site in this kinetically competent intermediate.

2. Experimental procedures

2.1. High-yield expression and purification of RTPR

The pKK223-3 plasmid (pSQUIRE) [53] bearing the *Lactobacillus leichmannii* RTPR gene was received as a generous gift from Dr. JoAnne Stubbe (MIT). The plasmid was transformed into BL21(DE3) competent cells (Stratagene) in accordance with the manufacturer's protocol. Colonies from the transformation were used to inoculate LB broth starter cultures, which were grown with ampicillin selection for 8 h at 37 °C with shaking. 48 custom-made 2L-capacity glass Erlenmeyer flasks with extra-large baffles were filled with 200 mL Terrific Broth (Sigma) and inoculated with 2 mL starter growth each. Cultures were grown with ampicillin selection at 37 °C with shaking (250 rpm) until OD_{600} reached the value of 2 (5 1/2 h). Cultures were then induced with isopropyl beta-D-1-thio-

galactopyranoside to the final concentration of 0.5 mM, allowed to rest for 15 min; temperature was then dropped to 16 °C and the cells were grown for additional 20 h with shaking (300 rpm). 120 g of cell paste were harvested by centrifugation at 4000 rpm and frozen at −80 °C until further processing.

We attribute this high yield to the use of the enriched medium, dramatically increased aeration achieved through combined effects of the special flasks and aggressive shaking, and the prolonged growth under gentle conditions.

Frozen cells were resuspended in lysis buffer (20 mM in potassium phosphate, 1 mM in EDTA, 1 mM in BME and 0.1 mM in PMSF, pH 7.2) and disrupted by passing twice through a pumped-fluid processor. Protein was purified through a sequence of protamine sulfate/ammonium sulfate fractionation, anion exchange chromatography (DE 52 resin, Whatman), and size exclusion chromatography (Superdex 75 resin, GE Healthcare). Protein was concentrated using Amicon concentrators (volume 500 mL, MWCO 50). Final protein yield was approximately 60 mg per liter culture, 90% pure. RTPR activity was assayed with the UV–Vis-coupled thioredoxin/thioredoxin reductase assay that is standard for this system [54] and found to be 1.2 μmol mg^{-1} min^{-1} (target level).

2.2. The RFQ technology

The layout diagram of the rapid freeze-quench apparatus is presented in Fig. 1. The apparatus consists of a commercially available constant-velocity syringe-driving ram (D) with a printed-circuit motor, a pulse programming unit (E) and solution delivery tubing (F) [40], and the following components designed and machined in-house: a Wiskind-type grid mixer, an ejection nozzle and a freeze-quenching block that includes copper-beryllium alloy wheels (J), scrapers and a copper sample collection basin. In brief, the reagents are expelled from the ram-driven syringes into the mixer (G), pass through an aging hose (H) whose length can be varied to control the age of the final sample, and are sprayed onto the rapidly rotating wheels kept at 80 K, where the reaction is quenched. The final product is in the form of frozen powder. It is transferred into the EPR tubes at the packing station (*vide infra*).

2.2.1. Ram and syringes

We have adapted a commercially available System 1000 constant-velocity syringe driving ram and PEEK solution delivery tubing. The pulse programming unit is capable of setting up a maximum of four pulses separated by delays whose duration may be varied between 0.01 s and 9900 s in increments of 0.01 s. Each pulse is assigned its own ram velocity. The ram is capable of velocities between 0.8 and 8.0 cm s^{-1}. Each pulse is also characterized by the vertical displacement of the ram: displacement can be set between 0.1 mm and 100 mm in increments of 0.1 mm.

We use 0.5 mL quartz syringe barrels. The small volume provides excellent control over the amount of ejected sample, but requires proportionately high ram speeds: the ram moves at 8 cm s^{-1}, corresponding to the linear velocity of the reacted solution of about 600 cm s^{-1} at the outlet from the aging hose.

To begin the experiments, the reagents are drawn into two to four (depending on the number of active reaction components) syringes that are mounted on the top of the constant velocity ram unit from Update Instruments. At the core of the ram unit is a programmable DC printed circuit servo motor, which maintains a rectangular ram acceleration profile under variable load and ensures uniform mass flow rate of the solutions.

When the reagents are drawn into the syringes, some air remains in the dead space. If not removed, this residual air, being compressible, leads to substantial deceleration in the velocity of the solutions when they are later expelled from the syringes, and at the end of the ejection the reaction mixture dribbles from the outlet nozzle, contaminating the frozen sample with droplets of unknown age. We bypass this problem by repeated cycles of manual filling and emptying of the syringes. Moreover, we noticed that in the process the gaskets on the syringe plungers may become damaged and later fail to withstand the immense pressures produced in the system during the ejection part of the cycle. We solved this problem by fabricating custom plungers secured with double Buna (N) gaskets positioned 3 mm apart on the shaft of the plunger. Through multiple trials of several materials we have found Buna (N) elastomer to possess the optimal combination of elasticity, hardness, and tear, abrasion and compression set resistance for use in the gaskets. We subjected the assembly to rigorous performance tests that demonstrated less than 1% failure (1 per 100 trials). This part of our design ensures uniform movement of the sample through the system, which translates into precise control over the age of the sample.

2.2.2. Mixer

We have used the classical Wiskind grid mixer design [55,56]. The sample syringes are laterally coupled to the mixer via pressure-resistant inert PEEK tubing in a T-shaped inlet arrangement. The inner chamber of the mixer is occupied by a stack of four stainless steel mixing grids made from mesh counting 250 lines per square inch (McMaster-Carr Supply, Cleveland OH). The grids are separated by Lucite plates with a central channel drilled through them. This channel has a volume of 1.6 μL and serves as a mixing chamber. The mixing is initiated when two incoming reagent streams impinge on each other, and is completed when the stream passes through and is disrupted by the fine mesh grids. High linear flow velocity (580 cm s^{-1}) leads to powerful turbulence in the chamber, where the Reynolds number would be well in excess of 3000 even in the absence of the mixing grids. This ensures efficient mixing without the clogging problems that plague some micromixer designs. The reaction is allowed to proceed in the aging tube that is connected to the outlet channel of the mixer. The extent of the reaction is controlled by the delay set on the pulse control unit.

2.2.3. Nozzle

Our ultimate goal was to obtain fine and uniformly quenched frozen sample powder. The rate at which heat is removed from a body is directly proportional to the surface area of the body and inversely proportional to its thickness. Therefore, to achieve rapid and uniform freezing of the sample jet as it impinges on the cryogen, it is desirable to atomize it into small even-sized particles. Small particles are also amenable to easy packing into the EPR sample tubes. With this in mind, an innovative ejection nozzle was designed and machined in our lab. (Fig. 2). It consists of a metal tube bent at a 90° angle, stopped at one end and on the other end attached through a tapped connector to the outlet of the aging tube. The long end of the metal tube is fixed parallel to the surface of the copper wheels (*vide infra*). 25 holes, each 100 μm in diameter, have been drilled into the bottom aspect of the tube. The nozzle tube was constructed out of a stainless steel medical syringe needle, Gauge 22, ID = 0.413 mm, OD = 0.7176 mm. In order to drill the holes, the needle was mounted on a piece of aluminum angle which in turn was mounted on the cross-slide of miniature lathe. The holes were made using drill bits mounted in the spindle of the lathe by a two step process. First, a 0.38 mm OD bit was used to drill out the outer conical depressions of approximately 0.25 mm diameter. Next, the holes were made using a 0.10 mm bit. All maneuvering of the lathe was done manually under a microscope with 10× magnification. The drilled nozzle tube was deburred and then attached to its mount using soft solder. The end of the nozzle was closed by soldering in a piece of the stainless

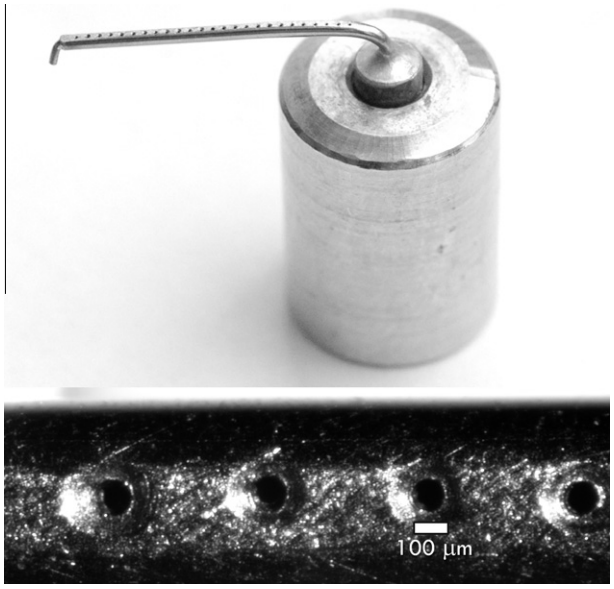

Fig. 2. Photograph of the RFQ nozzle. (Inset) micrograph of the holes in the nozzle tube with a scale bar.

steel wire of OD = 0.38 mm. Total cross-sectional area of the holes is equal to the cross-sectional area of the aging tube – therefore, the linear velocity of the solution is invariant as it passes from the aging hose through the nozzle. This design ensures that the back pressure in the system also does not increase (increase in backpressure causes the quartz syringes to rupture). However, because the stream is broken up into 25 jets, the contact area of the ejected solution and air is quadrupled. Due to their high kinetic energy, longer jet columns are unstable and fragment upon contact with molecules and particles of air.

For anaerobic work, anoxic atmosphere setup is envisaged, where the quench apparatus is placed in an air-tight glove box filled with nitrogen or another gas suitable for anaerobic work. The nozzle is positioned about 1.5 cm above the wheels. The spray impinges on the rotating wheels with the linear velocity of less than 6000 mm s^{-1}, and the thickness of the frozen sample is calculated to be 20 μm when the wheel dimensions and angular velocity are taken into account. Close positioning of the nozzle with respect to the wheels is advantageous because it obviates the need for conducting quench *in vacuo* or in low-pressure atmosphere that exists when the reaction is sprayed on/into the cooling medium directly from the mixer [46]. In ambient air, the thin reaction jet can be significantly slowed down and broken up by collisions with gas molecules, especially when the length of the jet is increased to achieve longer reaction times. This effect is negligible for the distance of 1.5 cm.

2.2.4. Wheels

The double-wheel design we use for quenching is analogous to that introduced by Lin and co-workers and Tanaka and co-workers for their microsecond regime studies [57,58]. The wheels were machined from two solid beryllium copper cylinders (diameter 43 mm, height 30 mm). Beryllium copper alloy, or beryllium bronze, retains the high thermal conductivity of pure copper, but is more resistant to abrasive scratching and deformation by indentation. As an additional benefit, at low temperature this material possesses high thermal conductivity and remains non-brittle [59,60]. Thanks to these properties, beryllium copper enjoys wide popularity in cryogenic applications, such as refrigeration and heat exchange.

The wheel cylinders are mounted on flexible horizontal axles and rotate in opposite directions such that the tangential component of the angular velocity vector at the top of one wheel is directed towards that of the other. The wheels do not touch each other. Each wheel is driven by its own servomotor and can rotate at speeds from 2000 to 15,000 rpm. The 2000 rpm speed is used for cooling the wheels by immersion in liquid nitrogen (*see* Section 2.2.5), and the 15,000 rpm speed is designated for the freeze-quench part of the cycle, ensuring (*see* Section 2.2.3. directly above) that the reaction solutions are deposited on the wheel in a layer whose calculated thickness is about 20 μm.

Prior to each use, the wheels are polished to smooth and lustrous finish using sandpaper of increasing grade, followed by buffing cloth. A commonly voiced concern about using copper in paramagnetic applications is that it might itself give an EPR signal (some abrasion of the wheel surface and deposition of the wheel material in the sample is, of course, unavoidable). In fact, there is indeed one report of a contaminating Cu(II) signal presumably arising from copper wheel flakes [61]. The wheels were used for a freeze-quench biological application. The type of alloy from which they had been manufactured was not specified. We have checked multiple samples for the well-known Cu(II) signal and have never detected it. The absence of paramagnetic copper in our samples has the following explanation. Metallic copper is magnetically transparent (individual atoms do possess a net magnetic moment but their random orientation and delocalization of the unpaired electrons over the metallic lattice result in zero net magnetization) [62,63]; to give an EPR signal, copper has to be oxidized – copper oxide and copper carbonate are two well-known compounds. The oxides are similar to those of aluminum in that, when formed, they are confined to the top layers of a piece of copper, and prevent bulk corrosion. Now, the highly conductive beryllium bronze used to machine the wheels of our apparatus is magnetically transparent and also is very resistant to oxidation [64], and is commonly used for applications in harsh chemical environments. Even in the unlikely event of oxide formation on the surface of the wheels, such formation would be very limited, and our practice of polishing and buffing the wheels before each experiment ensures that any such oxides are removed.

2.2.5. Scrapers, the quenching basin and sample production

The wheels are mounted directly above a quenching basin assembled from solid copper blocks and panels. The quenching basin rests on a movable platform (Fig. 3). The experimenter can vary the distance between the quenching basin and the wheels by turning a handle to displace the platform along the vertical axis. The quenching basin rests in an insulating polystyrene container. An identical container has been cut to form a tall lid covering the first one such that the two containers enclose both the basin and the wheels. Into the bottom of the lower container is tightly inserted a hose with a stopcock to provide an outlet for rapidly pouring off nitrogen. At the beginning of each quench cycle the wheels

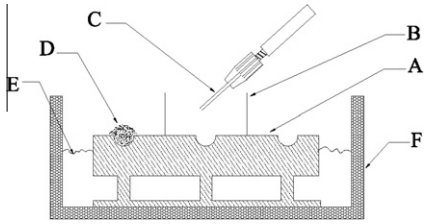

Fig. 3. Diagram of the packing stage. (A) Copper plate, (B) stainless steel post for pushing the sample into the tube, (C) D-band sample tube, (D) freeze-quenched sample ready for packing, (E) level of liquid nitrogen, (F) styrofoam vessel.

and the quenching basin are cooled to 77 K by immersion in liquid nitrogen. The 77 K point is reached when nitrogen boiling on the surface of the wheels stops, as has been verified via thermocouple measurements. Cessation of boiling provides a convenient visual signal for the experimenter and eliminates the need for thermocouple measurements during the preparation of the quenched samples.

Once the copper parts have been cooled to 77 K, three quarters of the volume of liquid nitrogen are rapidly drained from the assembly through the outlet in the polystyrene container. The particles produced by our freeze-quench apparatus are very fine and light. If the quenching basin remains fully immersed in nitrogen, the frozen particles quickly disperse in it and settle on the walls of the basin and the insulating container, precluding their collection. A layer of liquid nitrogen remaining in the container ensures that the assembly remains at the temperature near 77 K, which was verified by thermocouple measurements, and also generates an atmosphere of gaseous nitrogen that prevents water vapor in the ambient air from diluting the sample by deposition onto the cold metal parts.

Next, the reaction is ejected through the nozzle onto the rapidly rotating wheels. The frozen solution is continuously scraped off the wheels by precision stainless steel blades and falls into the quenching basin. The blades are brought into contact with the wheels just prior to ejection by elevating the platform on which the quenching basin stands. The samples thus prepared have the macroscopic consistency of very fine non-crystalline powder. Thanks to the presence of the blades the incoming solution always encounters cold metal with its superior thermal conductivity and not ice, which is a relatively good insulator. For our design, each double-edge blade is cut lengthwise, resulting in two single-edged blades. These are inserted into holders we manufactured in-house (*refer to* Fig. 1). The holders are mounted on the floor of the quenching basin at an approximately 30° angle to the horizontal plane. Each holder is supported mid-length by two small stiff springs. The springs ensure that the contact between the wheels and the blades is adequate for scraping off ice, but gentle and not damaging to the wheels. In order to ensure sharpness, the blades are changed after each RFQ use.

2.2.6. Temperature control

All parts of the apparatus that hold the reagents (syringes, mixer, and the tubing) can be fully enclosed by a water bath, should temperature control of the reaction be required. The water bath with a tight-fitting lid is mounted on top of the uppermost plate of the ram. Each of the syringe housings is supplied by Update Instruments with an attached external gasket. These gaskets serve to prevent leakage of fluid used for temperature control down onto the ram motor. The temperature bath in our lab is coupled to a circulator that has a working temperature range between −20 and +100 °C.

2.2.7. Sample packing

Our apparatus covers the millisecond time regime. One its chief advantages is its versatility: it produces samples in the physical form suitable for studies with multi-frequency EPR, as well as by nuclear magnetic resonance, resonance Raman, optical and Mössbauer spectroscopy. Examination of one sample by different techniques opens the exciting perspective of obtaining complementary sets of information.

Packing the frozen sample into D-band EPR tubes presents special challenges due to the tubes' small size: the commercially available tubes used for HF EPR have the internal diameter of 0.5 mm, the wall thickness of 0.05 mm or 0.1 mm.

To pack the sample into D-band EPR tubes, we have built a special packing stage (Fig. 3). Its largest component is a copper plate 70 mm thick with circular indentations used to hold the frozen sample powder. The indentations are 8 mm in diameter and 3 mm deep. Small (0.38 mm in diameter, 13.5 mm in height) upright stainless steel posts are vertically attached to the plate and are used for packing the sample. The packing stage is placed in a Styrofoam container and kept under liquid nitrogen, but not submerged, so that the top surface of the stage remains level with the liquid and dry. A clear acrylic plate is covers the top of the Styrofoam container to keep condensation from accumulating on the packing stage. This cover is moved slightly to admit access to the stage when the actual packing takes place. The frozen sample is transferred using a spatula also cooled in liquid nitrogen, from the quenching basin into the indentation on the packing stage. A D-band sample tube (quartz, outer diameter 0.7 mm, inner diameter 0.5 mm, purchased from VitroCom, Mountain Lakes, NJ) is secured in a clutch pencil-like implement with a four-jaw chuck. The assembly is cooled in liquid nitrogen; the free end of the D-band tube is tapped gently on the frozen sample powder. Next, the powder is pushed deep into the tube using the snugly fitting post of the packing stage. These steps are repeated until the entire volume of the tube is filled with the sample powder. Between the steps the tube assembly is immersed in liquid nitrogen. Packing factor of 0.5 was determined by melting the contents of the tube. After packing is complete, the chuck is opened, and the sample tube is placed in storage under liquid nitrogen. Using the chuck to secure the sample tube prevents warming of the sample through contact with the investigator's fingers as well as protects from liquid nitrogen burns. The sample tubes are quite robust using this setup, and breakage is relatively rare. Note that the total frozen sample volume resulting from each RFQ run is typically much greater than the individual EPR tube volume, so that if tube breakage does occur during sample packing another can easily be mounted and packed.

The acrylic cover combined with the constantly boiling nitrogen in the Styrofoam container combine to provide a relatively air- and water-free environment for the packing of the sample. However, the time window in not unlimited, and eventually liquid air will condense in the sample packing stage wells. On average, we find that samples must be completely packed within 10 min of immersing the stage in the liquid nitrogen.

To prepare samples for X-band EPR investigations, an X-band tube (quartz, outer diameter 4 mm, inner diameter 3 mm, purchased from Wilmad-Labglass, Buena, NJ) is attached to a glass funnel via a length of heat-shrink tubing. The assembly is immersed in a bath of isopentane kept at 130 K. This precaution prevents any dioxygen (boiling point, 90 K) that condenses into the tube under liquid nitrogen, from violently exploding during packing and expelling the packed sample. The sample powder is transferred from the quenching basin into the funnel using a liquid nitrogen-chilled spatula. The sample is then packed using a liquid nitrogen-chilled Teflon-tipped packing rod. Packing factor of 0.8 was determined by melting the contents of several tubes. The tubes containing the sample are then stored under liquid nitrogen.

All parts of the system that come in contact with the sample (hoses, packing stage, syringes) are washed and dried with compressed air between sample preparations.

2.3. Preparation of RTPR RFQ samples for EPR analysis

Immediately before rapid freeze-quench, suitable aliquots of RTPR were reduced with a concentrated solution of dithiothreitol (Sigma): dithiothreitol was added to RTPR to the final concentration of 30 mM. The mixture was incubated for 15 min at 37 °C. Next, DTT was removed from the mixture via two rounds of filtration-concentration in Amicon-Ultra 15 centrifugal filter devices (MWCO 50 K) until the desirable concentration of RTPR in the

retentate was achieved, as measured by UV–Vis. The molar absorption coefficient for RTPR is ε_{280} = 101,000 cm^{-1}. Two 0.5 mL syringes were mounted on the ram unit; one was filled with a solution containing 600 μM RTPR and 1.2 mM dGTP (Sigma), the other – with 900 μM AdoCbl (Sigma). Potassium phosphate buffer (100 mM and pH 7.5) was used for the preparation of solutions. All manipulations involving AdoCbl were performed in the dark or in the dim light to avoid cofactor photolysis. A 40-ms RFQ sample was prepared according to the procedures outlined in the Section 2.2 herein. RFQ sample had macroscopic consistency of very fine powder. This powder was packed into the X-band and D-band EPR tubes according to procedures outlined in the Section 2.2.7 herein, and stored under liquid nitrogen (77 K) until needed.

2.4. Procedure for simulating the EPR spectra

Procedure for simulating and fitting the EPR spectra arising from exchange- and dipole-coupled pairs was published elsewhere [20]. In summary, the electron Hamiltonian for the system of two unpaired electrons includes anisotropic electron Zeeman interactions, isotropic exchange interaction (J_{ex}) and anisotropic dipolar interaction (D). The electron Hamiltonian is solved by matrix diagonalization, and the eigenvectors and spin state energies are extracted. Eigenvectors and eigenenergies are used to calculate transition probabilities between the states and the expectation values. Each spin can be coupled one or two nuclei though hyperfine interaction. The hyperfine field is calculated using the spin expectation values obtained in the previous steps. Any of the above parameters can be varied independently or together until an optimal fit is achieved. In particular in the current system, the unpaired electron on Co(II) nucleus and the thiyl radical are both represented by anisotropic g tensors, and are coupled to the Co(II) nucleus (nuclear spin 7/2) and one β-proton nucleus from thiyl radical (nuclear spin 1/2).

The following parameters were varied to achieve satisfactory fits: the principal values of the thiyl radical g tensor, the magnitude of the exchange coupling, and the Euler angles relating the thiyl radical g tensor coordinate system to that of Co^{2+}. The fitting was done by trial and error. An optimal fit to the experimental data lead to a direct evaluation of the mutual orientation of and distance between the interacting spins.

In our simulations, the value of the anisotropic dipolar coupling is input as part of the electron Hamiltonian that is used to calculate the simulated spectra. Thus an optimal fit to the experimental data leads to direct evaluation of the mutual orientation of and distance between the interacting spins. These exchange coupled spin pairs have been also simulated in other systems [65–76].

3. Experimental results

3.1. Quality of mixing and instrument dead time assessment

The quality of mixing and the dead time of the instrument were assessed using the reaction of ferric myoglobin binding azide. This reaction has been extensively described in the literature [37,46,77–79]. The heme iron of ferric myoglobin (5 electrons in its d orbitals) exists in an octahedral ligand environment, and in the heme plane is ligated to four nitrogen atoms. The fifth coordination site (in the proximal pocket) is occupied by the nitrogen of an axial histidine. The occupant of the sixth coordination site (in the distal pocket) is variable and determines the energy separation between the upper and lower groups of d orbitals [80]. For example, a dissociable water molecule can act as such axial ligand [78,81]. Water is a weak ligand, so the separation between the groups of d orbitals is small, and iron is in the high spin (HS, S = 5/2) state with its diagnostic strong g = 6 EPR absorption [82]. Azide ion, a strong ligand, displaces the water molecule and forms a very stable complex with the heme iron [79], converting it to a low spin (LS, S = 1/2) form, with the concomitant replacement of the g = 6 signal by the rhombic line at around g = 2 [83,84].

We reacted 625 μmol equine skeletal muscle myoglobin (lyophilized powder purchased from Sigma) with 6.25 mM freshly prepared solution of sodium azide (powder purchased from Sigma), both in potassium phosphate buffer at pH 7.8. The reaction was allowed to proceed for preset times ranging between 5 ms and 180 ms before quench (at this stage, the reaction times were calculated from ram linear velocity and the length of the aging tube). The reaction was explored at two temperatures: 22 °C (20 data points) and 37 °C (50 data points). Samples where myoglobin solution was mixed with buffer with no azide present were also prepared (true zero-point samples, henceforth referred to as "zero-time shots"). We followed the disappearance of the HS heme iron signal by EPR spectroscopy (9 GHz, 77 K) by measuring peak-to-peak amplitude of the g = 6 portion of the signal. The 10-fold excess of azide in the mixture allowed us to make a pseudo-first-order rate law approximation. Natural logarithms of the intensity of EPR signal, excluding those from the zero-time shots, were plotted in the usual manner against the calculated age of the reaction at both temperatures (Fig. S1). The rate constants obtained from the fits to the data are very close to those reported in the literature under similar experimental conditions [41,85,154], *see* Table S1.

The fits were extrapolated back to the true zero-time data points. The time coordinate difference between the true zero time points and the y-intercept of the fit lines constitutes the dead time of the instrument [38]. The dead time was established to be about 30 ms (30 ms from the 37 °C plot, 27 ms from the 22 °C plot).

The experimentally determined dead time of 30 ms using the Update Instruments RAM in combination with the commercial Wiskind grid mixer and the self-built LN2/rotating wheel assembly is longer than the dead time of ~5 ms obtained using this RAM and mixer with cold isopentane as the freezing agent. The source of this additional dead time is not clear, as calculations indicate that freezing of the reaction mixture upon contact with the wheels occurs on the microsecond time scale. Moreover, use of microfluidic silicon mixers (appropriate for very short reaction times) in combination with the rotating wheels has yielded freeze times on the order of ~50 μs. We believe the additional dead time obtained when using the Update Instruments RAM/Wiskind grid mixer/rotating wheel assembly derives from reflection of some amount of material off of one wheel onto the other before freezing occurs. The velocity and volume of the reaction mixture exiting the mixer is such that some degree of "splashing" does occur, adding to the measured dead time of the apparatus. Efforts to confirm this as the dead time source and eliminate it are underway.

Next, the source of the modest variability in the samples generated by the RFQ system was investigated. Microscopic consistency of the zero-time samples is determined primarily by mixing; consistency of the reaction samples is determined by both mixing and freezing. By comparing the variance in the amplitude of the zero-time samples (0.0022) to that of the binding reaction time shots (0.07–0.1), we came to the conclusion that mixing, rather than freezing, is the primary source of the data point scatter. To improve on our current mixer performance, we are exploring new, more efficient mixer designs, with tangential inlet ports, finer mesh and reduced chamber volume. In parallel, we are investigating a possibility of machining the syringe barrel from stainless steel. The new mixer designs we have in mind all lead to increased pressure in the syringe barrels. Syringe barrels, as supplied by Update Instruments, are made from fused quartz, and currently place a limit on the reduction in the sizes of the downstream components.

Another source of variability is the packing factor. Even in the hands of a skilled experimenter the density of the packing will vary by at least 10–20%. Packing frozen sample in thin-walled EPR tubes is technically challenging: sample needs to be kept at a constant low temperature, free from frost deposition. Application of excessive packing force inevitably leads to breakage of the thin-walled of EPR tubes, and the sample is usually not recoverable, as it becomes mixed with transparent shards of quartz. This source of variability is extensively described in the literature [43,86] and is inherent in the process. Under current conditions it is not feasible to avoid it.

Overall, the use of this apparatus allows the generation of RFQ samples on the millisecond time scale which can be packed in the small diameter sample tubes which are used in pulsed and CW HFEPR. This apparatus has been used in a recent HF EPR study of catalase-peroxidase from *Mycobacterium tuberculosis* and its reaction intermediates [155] and is used in this work for the study of the exchange-coupled pair formed by ribonucleotide reductase from *L. leichmannii*.

3.2. HF EPR/RFQ of the exchange-coupled pair in ribonucleotide reductase from L. leichmannii

The X-band and the D-band spectra of the 40 ms RTPR RFQ sample of pre-reduced RTPR, AdoCbl and dGTP are presented in Figs. 4A and 5 respectively, along with the simulations thereof. The simulation parameters are listed in Table 1. In spite of using both the X-band and the D-band spectra to improve the reliability of fits to the experimental data, the problem remains underdetermined due to the number of adjustable parameters required for the simulations. Simultaneous fitting of the D- and X-band spectra has led to a refinement of the value of the exchange coupling and the thiyl radical *g*-values relative to the X-band spectrum alone, but it cannot be stated that the entire resulting parameter set constitutes a unique solution. For example, as evidenced from Fig. S3, the *g*-tensor principal values and orientation are to some degree correlated with respect to their influence on the D-band spectra. A more detailed characterization of the correlations between these and other spectral parameters is in progress. However, accurate simulations of both the X- and D-Band spectra require the refined J_{ex} and thiyl radical *g*-values given in Table 1, and thus the major structural conclusions reported here (see below) are supported.

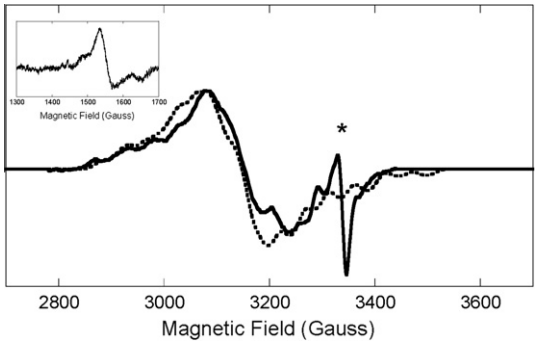

Fig. 4. X-band EPR spectrum and simulation of the exchange-coupled pair; (inset) half-field transition exhibited by the exchange-coupled pair. Sample age: 40 ms. For sample preparation details, *see* text. For simulation parameters, *see* Table 1. EPR instrumental parameters: frequency, 9.4420 GHz; MW power, 1 mW; temperature, 13 K; modulation frequency, 100 kHz; modulation amplitude, 8 G; time constant, 0.25 s; individual scan time, 1; number of scans, 2. (Inset) frequency, 9.2696 GHz; power, 1 mW; temperature, 77 K; modulation amplitude, 10 G; time constant, 0.25 s; individual scan time, 240 s; the displayed spectrum was accumulated from 4 scans. The asterisk denotes an unknown radical species not associated with the exchange-coupled pair.

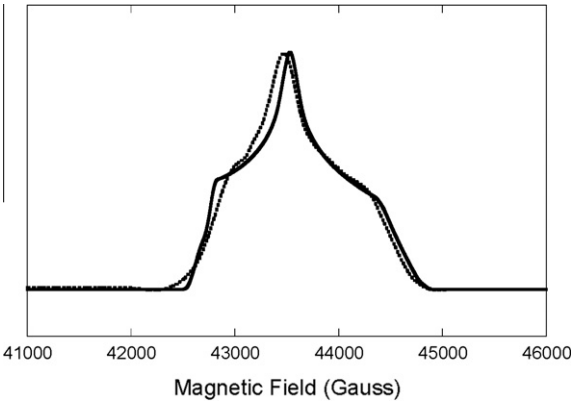

Fig. 5. D-band two-pulse echo-detected EPR spectrum and simulation of the exchange-coupled pair. Sample age: 40 ms. For sample preparation details, *see* text. For simulation parameters, *see* Table 1. Pulsed EPR instrumental parameters: frequency, 130.001 GHz; first pulse width, 40 ns; second pulse width, 80 ns; time between pulses, 150 ns; repetition rate, 8 kHz; averages per data point, 10,000; temperature, 7 K.

Inspection of the X-band spectrum reveals the spectroscopic hallmarks of the strongly exchange-coupled pair reported previously [16,20], where protein-bound cob(II)alamin interacts with the thiyl radical. The line is centered on the effective *g* value of 2.1 (approx. 3100 G), and displays cobalt nuclear hyperfine splittings of 50 G (nonenzymatically produced cob(II)alamin bound to the enzyme produces splittings of 110 G [27,87]). The half-field transition ($\Delta M_s = 2$) at approx 1550 G, diagnostic of dipolar coupled spin pairs [88,89,156–160], is present as well (Fig. 4 inset).

The D-band echo-detected EPR spectrum is shown in (Fig. 5). To our knowledge, this is the first HF pulsed EPR spectrum of an organic radical-cob(II)alamin exchange-coupled pair. To establish the identity of the species giving rise to the spectrum, we performed spectral simulations. As point of departure for our simulations, we started with the complete set of parameters from the 1996 study [20]. In 1996 the lower limit of J_{ex} was estimated to be 125 GHz (4.18 cm^{-1}) based on simulations of the X-band spectrum. In the present experiment, use of $|J_{ex}| = 125$ GHz also reproduces the X-band spectrum, but a satisfactory fit to the D-band spectrum can only be achieved with the use of $|J_{ex}| \geqslant 180$ GHz (6.00 cm^{-1}). When smaller values are used, the peaks arising from Co(II) and thiyl radical do not fuse into the experimentally observed single feature. Simulations with the value greater than 180 GHz (6 cm^{-1}) are not sensitive to the changes. As shown in Fig. 4, the value of 180 GHz is also used to deliver satisfactory simulation of the X-band spectrum. A clear illustration of the increased sensitivity of D-band relative to X-band spectra to larger values of $|J_{ex}|$ is given in Fig. S2.

Further constraints on the upper limit of the magnitude of J_{ex} comes from the Curie temperature variation studies. As demonstrated below, the thiyl radical and cob(II)alamin are antiferromagnetically coupled, hence the EPR-silent singlet is the ground state in this system, and the triplet is thermally populated. The fact that we and other workers are able to observe an EPR signal at the temperature as low as 6 K (*RT ca.* 50 GHz) [21] and even 2 K (*RT ca.* 17 GHz) [20], indicates that enough thermal energy is still available for the triplet state to be populated, and the energy gap separating the singlet and the triplet is at most 3–4 times greater than *RT* at these low temperatures [88,89]. Taken together, spectral simulations and temperature variation studies described below have converged on $J_{ex} \approx -180$ GHz (6.00 cm^{-1}).

The plot of the exchange-coupled pair's intensity of the EPR signal as a function of reciprocal temperature (Curie plot), normalized to the amplitude of $T = 6$ K data point is presented in Fig. 6. The

Table 1
EPR simulation parameters for the exchange-coupled pair in RTPR.

Parameters used in the present work	g_1	g_2	g_3	A_x	A_y	A_z	ϕ_{hyp}[a]	θ_{hyp}[a]	ψ_{hyp}[a]
Cob(II)alamin	2.230	2.235	2.009	15.0	36.0	310.0	50	0	0
Thiyl radical	2.200	2.09	2.025	107.0	98.8	96.4	−141	17	20
	J_{ex}	D	E	α_{dip}[b]	β_{dip}[b]	γ_{dip}[b]	α_g[c]	β_g[c]	γ_g[c]
	−6.00	-1.17×10^{-2}	3.33×10^{-3}	−76	63	62	90	−25	60

A values in MHz.
J_{ex}, D and E values in cm^{-1}.
[a] Euler angles relating hyperfine coupling principal axes to cob(II)alamin g principal axes.
[b] Euler angles relating dipole coupling principal axes to coba(II)alamin g principal axes.
[c] Euler angles relating thiyl radical g principal axes to coba(II)alamin g principal axes.

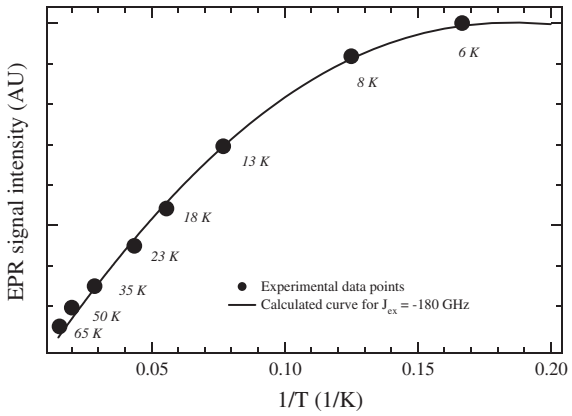

Fig. 6. Temperature dependence of the X-band EPR signal amplitude of the exchange-coupled pair formed in RTPR. For experimental parameters and calculation procedure, *see* text.

intensities of signals were assessed by measuring the peak-to-trough height in baseline-corrected spectra (linear correction only). At temperatures between 65 K and 18 K the Curie plot is almost linear. At temperatures below 18 K, the slope of the curve decreases. The dependence of the EPR signal amplitude A on temperature is described by relationship [88]

$$A = C\frac{3e^{\frac{J_{ex}}{KT}}}{1+3e^{\frac{J_{ex}}{KT}}}/T \quad (2)$$

where C is a material-specific temperature-independent constant. $C = 0.144$ K for thiyl radical–cob(II)alamin exchange-coupled pair was determined from a least-squares fit to the linear portion of the temperature dependence curve. A theoretical curve calculated using Eq. (2), with $C = 0.144$ K and $J_{ex} = -180$ GHz, and normalized to the amplitude of $T = 6$ K peak is also shown in Fig. 6. These data and calculations demonstrate that the spins comprising the exchange-coupled pair are antiferromagnetically coupled, with a ground singlet state and a thermally excited triplet state.The two-frequency approach provides the ability to validate the magnitude of the dipole–dipole coupling constant: the choice of simulation parameters must be identical at all frequencies. Both radicals were approximated as point dipoles [90]. Both the X-band and D-band spectra can be well reproduced in simulations using zero-field splitting parameters $D = 0.35$ GHz and $E = 0.1$ GHz.

One of the chief advantages of the two-frequency approach is the ability to emphasize the frequency-dependent terms by acquiring spectra at the higher frequency. In previous work, the values of g tensor were only approximated. In the current investigation, owing to the selective enrichment of the high-field spectra in the Zeeman terms of the Hamiltonian, it has been possible to fully resolve the anisotropy of the thiyl radical g tensor. Use of a new set of values for the g tensor, $g_x = 2.20$, $g_y = 2.090$, $g_z = 2.025$ is required to successfully reproduce the HF spectrum. The $g_x = 2.20$ value of the thiyl radical is on the smaller side of the range reported for thiyl radicals. Fig. S3 presents representative simulations in which the g-tensor principal values and orientations are varied.

A multifrequency EPR/simulation approach requires that the choice of simulation parameters be identical at all frequencies. To validate our new set of parameters, we used the entire set to simulate the X-band spectrum. The results are presented in Fig. 4A.

4. Discussion

4.1. Analysis of the thiyl radical g tensor values

By virtue of a greater sensitivity of the HF EPR to the field-dependent terms of the spin Hamiltonian, we have established a new, refined set of thiyl radical g values: $g_x = 2.20$, $g_y = 2.090$, $g_z = 2.025$. Although thiyl radicals are central to the catalysis of ribonucleotide reductases and pyruvate-formate lyase and pyruvate-formate activating enzyme, prior to the current study they have only been generated in model compounds or in proteins *via* UV or X-ray irradiation, and have also been studied *in silico* [91–98]. This work extends these previous studies and is the first application of HFPER/RFQ to characterization of a thiyl radical in a kinetically competent enzyme system.

Isolated thiyl radicals typically display approximately axially symmetric g tensors with relatively large $g_{//}$ (g_x) values and a $g\perp$ (with $g_y \approx g_z$) value in the vicinity of the free electron g factor of 2.002319. The properties of a g tensor may be understood by examining the environment of the unpaired electron. The large value of the $g_{//}$ in the case of sulfur radical is a result of the large spin–orbit coupling of sulfur: the spin–orbit coupling sharply increases with atomic number, and is only about 0.4 cm^{-1} for hydrogen, 70 cm^{-1} for oxygen, but reaches the value of 382 cm^{-1} for the sulfur atom [99,100]. The 3*s* orbital and the two 3*p* orbitals of cysteine in a thiyl radical are sp^2-hybridized and arranged at about 120° to each other in a plane [91]. The unpaired electron is located in the remaining 3*p* orbital, which is directed perpendicular to the hybrid plane. The $g_{//}$ component of the g tensor is assumed to be along the direction of the C-S bond. In an isolated thiyl radical, as a consequence of the symmetry of molecular orbitals, the sulfur lone pair orbitals are degenerate and the radical exhibits axial symmetry [97,101]. It has been shown that when one of the lone pairs engages in hydrogen bonding, the degeneracy is lifted, and the system assumes rhombic symmetry, i.e. the $g\perp$ component separates into g_y and g_z. Due to the polarity-induced changes in the electron density distribution geometry, and to the effects on *p–d* hybridization, hydrogen bonding also has a pronounced influence on the magnitude of the g_x value [102,103]. g_x values as high as 2.493 have been observed and calculated for cysteine-based thiyl radicals in non-polar environments [101,104]. g_x values are shifted to 2.29–2.15 in polar environments [102–105], an effect of hydrogen bonding analogous to that observed for tyrosyl

radicals [104,106]. g_x = 2.20 determined in our study is, therefore, consistent with a hydrogen-bonded thiyl radical. Although the details of this interaction and its full significance remain to be elucidated, this finding is intriguing. It is well understood that enzymes that utilize radicals in catalysis exert stringent control over these reactive species [107], and hydrogen bonding has been suggested as a factor that has a potential to modulate catalytic activity of radical enzymes [108–112]. For example, it has been experimentally demonstrated that hydrogen bonds play a catalytic role by positioning tyrosyl radicals for the cyclooxygenase reaction of prostaglandin synthase [113,114]. Hydrogen bond-mediated alignment of the reacting species with respect to one another and with respect to the catalytic active site residues was hypothesized to contribute to the rate enhancement *via* the reduction in the number of degrees of freedom available to the reaction participants [115,116] and the consequent decrease in the *entropy* of the ground state (compared to the state where the reaction participants are not fixed in place). Other things being equal, this decrease in entropy leads to lowered *energy* of activation. It was also recently proposed, based on high-resolution crystal structures, that a *network* of hydrogen bonds [117] is strategically deployed by serine protease to position the intermediates in the active site and/or stabilize the transition state [118,119]. While these studies provide an exciting context, it is imperative to identify hydrogen-bonding partner of the cysteine before firm conclusions regarding the catalytic significance of the hydrogen bond can be reached.

Assuming that the proton which is hydrogen bonded to the thiyl radical is exchangeable, it may be expected that the exchange-coupled spectrum resulting from RTPR samples prepared in H_2O and D_2O would show differences, but these differences have not been observed in X-band spectra [16]. The reason for this may lie in the relatively small size of the hyperfine coupling combined with the other sources of inhomogeneous broadening present in the spectra. The size of the hyperfine coupling of a hydrogen-bonded proton or deuteron coupled to a thiyl radical has not been determined, particularly under the conditions of the thiyl radical being exchanged coupled to a second electron spin species. However, an approximate value can be estimated from the measured hyperfine coupling of hydrogen-bonded deuterons to the oxygen of tyrosyl radicals. With a spin density of approximately 0.3 on the oxygen of tyrosyl radicals, hydrogen-bonded deuterons experience a hyperfine coupling of ~0.5 G [106], which would convert to ~3 G for protons. Scaling this to a spin density of 1.0 would give a hyperfine coupling of ~10 G for a proton coupled to a thiyl radical. Although this is a substantial coupling, it is small relative the other sources of broadening in the electron–electron coupled spectrum and thus may go undetected upon deuteration. Note that the substitution of two β-protons on cysteine, one of which experiences a hyperfine coupling of over 30 G to the thiyl radical, produced only a subtle narrowing of the individual spectral components of the exchange-coupled spectrum [20]. Thus it is possible that the substantially smaller coupling to the single hydrogen-bonded proton may have gone undetected in the X-band spectra. It is possible that S-band or ENDOR spectroscopy may successfully detect the presence of the hydrogen bond.

4.2. Determination of the spin multiplicity of the ground state of the exchange-coupled pair, and the magnitude of J_{ex}

Ribonucleotide reductase from *L. leichmannii* activates C–Co bond of the AdoCbl cofactor and generates the catalytically relevant thiyl radical even in the absence of substrate, as long as an allosteric effector is present. This incomplete yet catalytically competent system is an invaluable tool for the study of AdoCbl- and radical-based catalysis. The unpaired electron on Co(II) ion of the homolysed cofactor and thiyl radical are coupled through exchange and dipolar interactions [20]. The exchange interaction is represented by the Heisenberg–Dirac–van Vleck Hamiltonian

$$\widehat{H}_{ex} = -J_{ex}\widehat{S}_1 \cdot \widehat{S}_2 \tag{3}$$

where J_{ex}, the coupling parameter, is related to the extent of the orbital overlap. Orbital overlap that mixes the electronic wavefunctions and leads to the exchange interaction can be direct, or, in the case of superexchange, be mediated through bridging ions or delocalized electronic states that provide the conduit for spin–spin coupling [120–122]. When ground state $J_{ex} < 0$ (antiferromagnetic coupling), the spins are paired, the total spin of the system is $S = 0$, and the spin multiplicity $(2S + 1)$ is one: this is a singlet state. When $J_{ex} > 0$ (ferromagnetic coupling), the spins are parallel, the total spin is $S = 1$ with the multiplicity of three: a triplet state. The energy of singlet–triplet splitting is given by the magnitude of J_{ex}. The magnitude of J_{ex} has a profound effect on the appearance of EPR spectra. In the case of strong exchange coupling, such as that in RTPR, the g values of the individual spins blend into a joint, or "effective", g value – this effective g value for the thiyl radical and the unpaired electron of Co(II) is about 2.1 [67]. Since the exchange interaction is influenced both by the details of molecular structure, and by the distance between paramagnets, its interpretation and derivation of mechanistic conclusions is not straightforward [123,124]. The execution of such task is greatly aided by the information contained in the dipole–dipole coupling parameter D, which allows the exchange interaction to be placed into a structural context.

The through-space dipole–dipole interaction of the spins is described by the Hamiltonian

$$\widehat{H}_{dip} = 2\widehat{S}_1 \cdot D \cdot \widehat{S}_2 \tag{4}$$

The dipole interaction is proportional to $3\cos^2\theta - 1/r^3$, where r is the interspin distance and θ is the angle between the imaginary line connecting the electrons and the direction of the applied magnetic field. This clear dependence of the dipole interaction on distance and orientation engenders its utility for structural analysis. As a consequence, this parameter has been successfully utilized to describe the arrangement of spin pairs in many systems of biological interest [65–76]. In the case of RTPR, D is 0.35 GHz, corresponding to the interspin distance of about 6.5 Å, and simulations indicate the angle between the corrin ring normal and the interspin vector is approximately 60 degrees. $J_{ex} = -180$ GHz determined in the present study is stronger than would be predicted from simple distance considerations for two unconnected spins: J_{ex} is a function of orbital overlap, and has an inverse exponential dependence on the distance between the paramagnets, unless they are linked *via* an additional communication pathway.

Results from relevant literature examples presented in Table 2 indeed demonstrate the range of values that J_{ex} can take when spins are separated by 5–8 Å. The exchange interaction observed in several biological systems is significantly smaller than the one revealed in the present work for the exchange-coupled pair in RTPR. For example, an exchange coupling between tyrosyl radical and diferric cluster in a class I RNR has the interspecies distance of about 8 Å – and yet the lower limit for J_{ex} is estimated to be only 0.14 GHz [125]. On the other hand, J_{ex} for synthetic π-delocalized radicals that are directly coordinated to a metal atom, such as those prepared and investigated by Richardson and Kreilick [126,127], are on the order of 4–5 × 10^3 GHz for a similar interspin distance. The magnitude of the exchange interaction measured in this work is between these two extremes: it is larger than that expected for "isolated" radical separated by 6–7 Å but smaller than observed for radicals directly ligated to metal ions or biradicals linked covalently via a π system. Based on the magnitude and sign

Table 2
Literature data on the exchange interactions between species positioned 5-9 Å from each other.

System	Paramagnetic species	Distance between species (Å)	J_{ex} (cm^{-1})	Reference
Meta-pyridyliminonitroxide coordinated to Cu(hexafluoroacetonate)$_2$	Nitroxide and copper atom	6	−160	[126]
Para-pyridyliminonitroxide coordinated to Cu(hexafluoroacetonate)$_2$	Nitroxide and copper atom	4.6	−163.5	[126]
Meta-pyridylnitronylnitroxide coupled to Cu(hexafluoroacetonate) in solution	Nitroxyl radical and copper atom	5.25	−160 ± 5	[148]
Iron-semiquinone complex in *Rhodopseudomonas viridis*	Unpaired electron of the reduced primary quinone Q^{1-} and Fe(II)	6.2–7.8	0.12 ± 0.03 (sign not determined)	[149]
Spin(nitroxide)-labeled derivative of EDTA complexed to Cr(III)	Nitroxyl radical and Cr(III)	7.5 (or 10)	−0.006 (or + 0.008)	[150]
Spin(nitroxide)-labeled derivative of EDTA complexed to Fe(III)	Nitroxyl radical and high-spin Fe(III)	7.5	0.013	[150]
Spin(nitroxide)-labeled derivative of EDTA complexed to Mn(III)	Nitroxyl radical and Mn(II)	8.5	−0.004 (lower limit)	[150]
Spin-labeled (nitroxide) Fe(III) tetraphenylporphyrin with bromide as the fifth ligand	Nitroxyl radical and high-spin Fe(III)	8	−0.034 or 0.045 depending on the mutual orientation of the interspin vector and the iron z axis.	[151]
Synthetic material: spin-labeled (nitroxide) Fe(III) tetraphenylporphyrin	NItroxyl radical and low-spin Fe(III)	7	±|0.25 ± 0.05|	[152]
Spin(nitroxide)-labeled Cyt P450	Nitroxyl radical and low spin Fe(III)	7	±0.03	[152]
Ribonulcleotide reductase from *E. coli*	Tyrosyl radical and diferric cluster	About 8	0.0047 ± 0.0003	[125]
B12-dependent glutamate mutase from *Clostridim cochlearium*	4-glutamyl radical and cob(II)alamin	6.6 ± 0.9	0.13–3.4	[65]
Diol dehydrase and an adenosylcobalamin analog	Anhydroadenosyl radical (carbon-based) and cob(II)alamin	3	40–50	[74]
Ethanolamine ammonia lyase and ethanolamine	Carbon-based substrate radical and cob(II)alamin	8.7	−0.005	[153]
Lysine 5,6-aminomutase with substrate analog 4-thia-L-lysine	A transient and a persistent radical. Both are carbon-based radicals interacting with cob(II)alamin	7 for transient radical and 10 for persistent	0.4 for transient and 0.05 for persistent	[76]
Ribonulcleotide reductase from *Lactobacillus leichmannii*	Cysteine-based thiyl radical and cob(II)alamin	6–7	−6.00	Present work

of the exchange coupling measured here (J_{ex} = −180 GHz (6 cm^{-1})), it is proposed that the exchange interaction between Co(II) and thiyl radical in RTPR is mediated by a superexchange pathway [99,100,120,128–130]. Overall, the results of the two-frequency EPR study and the variable temperature study are consistent with the presence of intervening atoms or molecules between the catalytically active thiyl radical species and one of the products of AdoCbl homolysis (cob(II)alamin).

Recently, there has been a resurgence of interest in the idea that AdoCbl-containing enzymes create a finely tailored electrostatic environment in their active sites [112,131–137]. Evidence from *in silico* studies, reinforced with the analysis of site-directed point mutants, is strongly in favor of side chains of amino acids such as tyrosine [112] and glutamate [131,138] playing an supportive role in catalysis. There is a general lack of consensus on how this role is fulfilled mechanistically. For example, a recent QM/MM study of MMCM, which also uses AdoCbl in catalysis, has demonstrated strong hydrogen-bonding interactions between an active site glutamate residue and one of the oxygen atoms on the AdoCbl ribose moiety [139]. These interactions were shown to contribute 3.6 kcal mol^{-1} to the destabilization of Co(III) ground state and 9.1 kcal mol^{-1} to the stabilization of the transition state in the C–Co bond cleavage reaction, which is a significant effect considering that the C–Co BDE is around 30 kcal mol^{-1}, so a reduction of *ca.* 15 kcal mol^{-1} is required to account for the observed 10-orders-of-magnitude catalytic enhancement. Another group of authors in a theoretical study of MMCM and GM suggested a role for a conserved tyrosine residue [137]. They hypothesize that the tyrosine donates one electron to AdoCbl, generating a high-energy AdoCbl· intermediate.

In addition to the amino acids donated by the enzyme active site, ribose moiety of Ado· and the *d* orbitals of the cobalt atom have been proposed to contribute to the acceleration of the C–Co bond cleavage and to the overall progress of the reaction [140–146]. The strength of the spin exchange interaction measured in this work ($|J_{ex}|$ = 180 GHz, or 6 cm^{-1}, 17 cal mol^{-1}) is clearly too small to have a direct impact on catalysis or intermediate stabilization. Rather, it may lend indirect support, through its reporting of a superexchange interaction, for the viability of other proposed interactions. A DFT investigation into the origin of the large catalytic effect on the C–Co bond cleavage [142] demonstrated attractive interaction between the 2′-hydroxyl group of the adenosyl and the cobalt atom. It was suggested that the essence of the catalytic effect lies in the coupling of the homolysis step to the next reaction steps, which is possible because the reacting fragments do not have the chance to fully separate. Additionally, the authors calculated that the homolysed state is stabilized by 4 kcal mol^{-1} *via* the interactions of adenosyl radical with a residue in the active site. Jensen and Ryde [143] estimated a contribution of 14 kcal mol^{-1} to the observed catalytic effect to arise from the attractive interaction of the polar ribose group with Co(II) in the dissociated state. In addition, these authors in their QM/MM calculations observed a 10 kcal mol^{-1} stabilization of the Co(II) state by electrostatic interactions with unidentified residues in the active site of glutamate mutase, another AdoCbl dependent enzyme that relies on Co–C bond homolysis for its catalytic activity.

Several *in vitro* studies also pointed to an interaction between AdoCbl, its hydrogen abstraction substrate and the active site residues. Upon investigating the effect on the homolysis process of MMCM of site-directed mutagenesis and isotopic substitution of the 5′ hydrogen of AdoCbl, Vlasie and Banerjee [112] arrived at the qualitative conclusion that an active site tyrosine residue may play a role of a "molecular wedge" by stabilizing the deoxyadenosyl radical and/or hydrogen bonding to the substrate (of which RTPR's Cys 408 would be a functional analogue). Likewise, Jones and co-authors [147] demonstrated that AdoCbl photolysed in the active site of EAL was not sensitive to the magnetic field effects, in contrast to the behavior of the cofactor free in solution. They attributed this result to the coupling by the enzyme active site of the homolysis and hydrogen abstraction into one concerted step, emphasizing the favorable role played by the active site environment.

These latest efforts to identify the physical basis for enzyme-facilitated chemistry provided the theoretical context for the present work. An intact RTPR system and the combination of RFQ and HFEPR have been used to study a kinetically competent catalytic intermediate. The results constitute a first direct experimental indication that, in the course of catalysis by RTPR, the protein active site presents the reacting molecules with an environment that includes a hydrogen bond to the thiyl radical and intervening residues or solvent mediating an exchange coupling between the thiyl radical and cob(II)alamin. Identification of the molecules responsible for these interactions remains for future work, but their presence indicates the possibility of the enzyme providing specific contacts in a highly structured active site.

Acknowledgments

This work was funded by the National Institutes of Health (NIH) Grant GM075920 to G.J.G. J.M. was supported by AECOM Medical Scientist Training Program Grant No. 5T32GM007288. Prof. JoAnne Stubbe of MIT is thanked for the kind gift of pSQUIRE plasmid. Dr. Ronald D. Seidel (AECOM) is thanked for his assistance in RTPR expression and purification. Mr. Mike Cammer and AECOM AIF are thanked for the help in producing the image of the nozzle (Fig. 2).

Appendix A. Supplementary material

Supplementary data associated with this article can be found, in the online version, at doi:10.1016/j.jmr.2011.08.030.

References

[1] A. Jordan, P. Reichard, Ribonucleotide reductases, Annu. Rev. Biochem. 67 (1998) 71–98.
[2] J. Stubbe, W.A. van der Donk, Protein radicals in enzyme catalysis, Chem. Rev. 98 (1998) 705–762.
[3] M. Kolberg, K.R. Strand, P. Graff, K.K. Andersson, Structure, function, and mechanism of ribonucleotide reductases, Biochim. Biophys. Acta (BBA) – Proteins Proteomics 1699 (2004) 1–34.
[4] P. Nordlund, P. Reichard, Ribonucleotide reductases, Annu. Rev. Biochem. 75 (2006) 681–706.
[5] D. Lembo, W. Brune, Tinkering with a viral ribonucleotide reductase, Trends Biochem. Sci. 34 (2009) 25–32.
[6] H. Eklund, U. Uhlin, M. Färnegårdh, D.T. Logan, P. Nordlund, Structure and function of the radical enzyme ribonucleotide reductase, Prog. Biophys. Mol. Biol. 77 (2001) 177–268.
[7] J.C. Wilson, Study of Protein Structural Disorder by Electron Paramagnetic Resonance, Albert Einstein College of Medicine, PhD Dissertation, 2008.
[8] M.D. Sintchak, G. Arjara, B.A. Kellogg, J. Stubbe, C.L. Drennan, The crystal structure of class II ribonucleotide reductase reveals how an allosterically regulated monomer mimics a dimer, Nat. Struct. Biol. 9 (2002) 293.
[9] P. Reichard, From RNA to DNA, why so many ribonucleotide reductases?, Science 260 (1993) 1773–1777
[10] J. Stubbe, Ribonucleotide reductases in the twenty-first century, Proc. Natl. Acad. Sci. USA 95 (1998) 2723–2724.
[11] M. Fontecave, Ribonucleotide reductases and radical reactions, Cell. Mol. Life Sci. 54 (1998) 684–695.
[12] P. Reichard, Ribonucleotide reductases: substrate specificity by allostery, Biochem. Biophys. Res. Commun. 396 (2010) 19–23.
[13] R.H. Abeles, W.S. Beck, The mechanism of action of cobamide coenzyme in the ribonucleotide reductase reaction, J. Biol. Chem. 242 (1967) 3589–3593.
[14] H.P.C. Hogenkamp, Enzymatic reactions involving corrinoids, Annu. Rev. Biochem. 37 (1968) 225.
[15] Y. Tamao, R.L. Blakley, Direct spectrophotometric observation of an intermediate formed from deoxyadenosylcobalamin in ribonucleotide reduction., Biochemistry 12 (1973) 24–34.
[16] W.H. Orme-Johnson, H. Beinert, R.L. Blakley, The electron paramagnetic resonance spectrum of "active coenzyme B12", J. Biol. Chem. 249 (1974) 2338–2343.
[17] J. Stubbe, D. Ackles, R. Segal, R. Blakley, On the mechanism of ribonucleoside triphosphate reductase from *Lactobacillus leichmannii*. Evidence for 3′ C–H bond cleavage, J. Biol. Chem. 256 (1981) 4843–4846.
[18] J.A. Stubbe, Mechanism of B12-dependent ribonucleotide reductase, Mol. Cell. Biochem. 50 (1983) 25–45.
[19] G.W. Ashley, G. Harris, J. Stubbe, The mechanism of *Lactobacillus leichmannii* ribonucleotide reductase. Evidence for 3′carbon–hydrogen bond cleavage and a unique role for coenzyme B12, J. Biol. Chem. 261 (1986) 3958–3964.
[20] G.J. Gerfen, S. Licht, J.P. Willems, B.M. Hoffman, J. Stubbe, Electron paramagnetic resonance investigations of a kinetically competent intermediate formed in ribonucleotide reduction: evidence for a thiyl radical–cob (II)alamin interaction, J. Am. Chem. Soc. 118 (1996) 8192–8197.
[21] S. Licht, G.J. Gerfen, J. Stubbe, Thiyl radicals in ribonucleotide reductases, Science 271 (1996) 477–481.
[22] M. Goulian, W.S. Beck, Purification and properties of cobamide-dependent ribonucleotide reductase from *Lactobacillus leichmannii*, J. Biol. Chem. 241 (1966) 4233–4242.
[23] R.L. Blakley, Estimation of the enzymic formation of purine and pyrimidine deoxyribonucleotides by the use of the diphenylamine reagent, J. Biol. Chem. 241 (1966) 176–179.
[24] E. Vitols, C. Brownson, W. Gardiner, R.L. Blakley, A kinetic study of the ribonucleotide reductase of *Lactobacillus leichmannii*, J. Biol. Chem. 242 (1967) 3035–3041.
[25] B.P. Hay, R.G. Finke, Thermolysis of the Co–C bond in adenosylcobalamin (coenzyme B12)–IV. Products, kinetics and Co–C bond dissociation energy studies in ethylene glycol, Polyhedron 7 (1988) 1469–1481.
[26] R. Yamada, Y. Tamao, R.L. Blakley, Cobamides and ribonucleotide reduction. Degradation of 5′-deoxyadenosylcobalamin by ribonucleoside triphosphate reductase and binding of degradation products to the active center, Biochemistry 10 (1971) 3959–3968.
[27] J.A. Hamilton, R. Yamada, R.L. Blakley, H.P.C. Hogenkamp, F.D. Looney, M.E. Winfield, Cobamides and ribonucleotide reduction. VII. Cob(II)alamin as a sensitive probe for the active center of ribonucleotide reductase, Biochemistry 10 (1971) 347–355.
[28] O. Burghaus, M. Rohrer, T. Gotzinger, M. Plato, K. Mobius, A novel high-field/high-frequency EPR and ENDOR spectrometer operating at 3 mm wavelength, Meas. Sci. Technol. 3 (1992) 765–774.
[29] K. Mobius, Special volume: high-field and high frequency electron paramagnetic resonance, Chem. Soc. Rev. 29 (2000) 129–139.
[30] W.R. Hagen, Special volume: high-field and high frequency electron paramagnetic resonance, Dalton Trans. (2006) 4415–4434.
[31] M. Bennati, C.T. Farrar, J.A. Bryant, S.J. Inati, V. Weis, Pulsed electron-nuclear double resonance (ENDOR) at 140 GHz, J. Magn. Reson. 138 (1999) 232.
[32] M. Ubbink, J.A.R. Worrall, G.W. Canters, E.J.J. Groenen, M. Huber, Paramagnetic resonance of biological metal centers, Annu. Rev. Biophys. Biomol. Struct. 31 (2002) 393.
[33] K.K. Andersson, P.P. Schmidt, B. Katterle, K.R. Strand, A.E. Palmer, S. Lee, E.I. Solomon, A. Gräslund, A. Barra, Examples of high-frequency EPR studies in bioinorganic chemistry, J. Biol. Inorg. Chem. 8 (2003) 235–247.
[34] M. Bennati, T.F. Prisner, New developments in high field electron paramagnetic resonance with applications in structural biology, Rep. Prog. Phys. 68 (2005) 411–448.
[35] P.J. van Kan, E. Horst, E.J. Reijerse, P.J. Bentum, W.R. Hagen, Multi-frequency EPR spectroscopy of myoglobin. Spectral effects for high-spin iron (III) ion at high magnetic fields, J. Chem. Soc., Faraday Trans. 94 (1998) 2975–2978.
[36] R.M. Wood, D.M. Stucker, L.M. Jones, W.B. Lynch, S.K. Misra, J.H. Freed, An EPR study of some highly distorted tetrahedral manganese(II) complexes at high magnetic fields, Inorg. Chem. 38 (1999) 5384–5388.
[37] R.C. Bray, Sudden freezing as a technique for the study of rapid reactions, Biochem. J. 81 (1961) 189–195.
[38] R.C. Bray, Quenching by squirting into cold immiscible liquids, in: B. Chance, R.H. Eisenhardt, A.H. Gibson, K.K. Lonberg-Holm (Eds.), Rapid Mixing and Sampling Techniques in Biochemistry, Academic, New York, 1964, pp. 195–302.
[39] R.C. Bray, G. Palmer, H. Beinert, Direct studies on the electron transfer sequence in xanthine oxidase by electron paramagnetic resonance spectroscopy. II. Kinetic studies employing rapid freezing, J. Biol. Chem. 239 (1964) 2667–2676.
[40] R.E. Hansen, H. Beinert, Syringe ram for a rapid-freeze sampling instrument, Anal. Chem. 38 (1966) 484–487.
[41] D.P. Ballou, G.A. Palmer, Practical rapid quenching instrument for the study of reaction mechanisms by electron paramagnetic resonance spectroscopy, Anal. Chem. 46 (1974) 1248–1253.

[42] A. Tsai, V. Berka, R.J. Kulmacz, G. Wu, G. Palmer, An improved sample packing device for rapid freeze-trap electron paramagnetic resonance spectroscopy kinetic measurements, Anal. Biochem. 264 (1998) 165–171.
[43] S. de Vries, Freeze-quench kinetics, in: R.A. Scott, C.M. Lukeheart (Eds.), Applications of Physical Methods to Inorganic and Bioinorganic Chemistry, John Wiley & Sons, Ltd., 2007.
[44] G. Palmer, R.C. Bray, H. Beinert, Direct studies on the electron transfer sequence in xanthine oxidase by electron paramagnetic resonance spectroscopy, J. Biol. Chem. 239 (1964) 2657–2666.
[45] P. Moenne-Loccoz, C. Krebs, K. Herlihy, D.E. Edmondson, E.C. Theil, B.H. Huynh, T.M. Loehr, The ferroxidase reaction of ferritin reveals a diferric mu-1, 2 bridging peroxide intermediate in common with other O2-activating non-heme diiron proteins, Biochemistry 38 (1999) 5290–5295.
[46] A.V. Cherepanov, S. De Vries, Microsecond freeze-hyperquenching: development of a new ultrafast micro-mixing and sampling technology and application to enzyme catalysis, Biochim. Biophys. Acta – Bioenerg. 1656 (2004) 1–31.
[47] A.V. Harreveld, J. Crowell, Electron microscopy after rapid freezing on a metal surface and substitution fixation, Anat. Rec. 149 (1964) 381–385.
[48] J. Heuser, Quick-freeze, deep-etch method of preparing samples for 3-D electron microscopy, Trends Biochem. Sci. 6 (1980) 64–68.
[49] J.E. Heuser, Development of the quick-freeze, deep-etch, rotary-replication technique of sample preparation for 3-D electron microscopy, Prog. Clin. Biol. Res. 295 (1989) 71–83.
[50] J. Dubochet, M. Adrian, J. Chang, J. Homo, J. Lepault, A.W. McDowall, P. Schultz, Cryo-electron microscopy of vitrified specimens, Q. Rev. Biophys. 21 (1988) 129–228.
[51] Y.S. Song, D. Adler, F. Xu, E. Kayaalp, A. Nureddin, R.M. Anchan, R.L. Maas, U. Demirci, Vitrification and levitation of a liquid droplet on liquid nitrogen, Proc. Natl. Acad. Sci. 107 (2010) 4596–4600.
[52] B. Gottfried, C. Lee, K. Bell, The leidenfrost phenomenon: film boiling of liquid droplets on a flat plate, Int. J. Heat Mass Transfer 9 (1966) 1167–1188.
[53] S. Booker, J. Stubbe, Cloning, sequencing, and expression of the adenosylcobalamin-dependent ribonucleotide reductase from *Lactobacillus leichmannii*, Proc. Natl Acad. Sci. USA 90 (1993) 8352–8356.
[54] R.L. Blakley, Ribonucleoside triphosphate reductase from *Lactobacillus leichmannii*, in: P.A.H. Jones, M. Ellen (Eds.), Purine and Pyrimidine Nucleotide Metabolism, 51st ed., Academic Press, 1978, pp. 246–259.
[55] H.K. Wiskind, A uniform gradient turbulent transport experiment, J. Geophys. Res. 67 (1962) 3033–3048.
[56] H. Wiskind, On the application of fluid dynamics to the development of rapid mixing techniques, in: Rapid Mixing and Sampling Techniques in Biochemistry, Academic Press, Philadelphia, 1964, pp. 355–361.
[57] Y. Lin, G.J. Gerfen, D.L. Rousseau, S. Yeh, Ultrafast microfluidic mixer and freeze-quenching device, Anal. Chem. 75 (2003) 5381–5386.
[58] M. Tanaka, K. Matsuura, S. Yoshioka, S. Takahashi, K. Ishimori, H. Hori, I. Morishima, Ultrafast microfluidic mixer and freeze-quenching device, Biophys. J. 84 (2003) 1998–2004.
[59] A. Woodcraft, R.V. Sudiwala, R.S. Bhatia, The thermal conductivity of C17510 beryllium-copper alloy below 1 K, Cryogenics 41 (2001) 603–606.
[60] N. Arsent'eva, L. Zheleznyak, A. Snigirev, O. Dashkevich, A. Miller, E. Kuz'mina, Achievement of high requirements for rod and bar of structural-grade and electrotechnical bronze, Metallurgist 51 (2007) 232–236.
[61] N.P. Belevich, M.L. Verkhovskaya, M.I. Verkhovsky, in: Mitochondrial Function, Part A: Mitochondrial Electron Transport Complexes and Reactive Oxygen Species, Academic Press, 2009, pp. 75–93.
[62] M. Misono, W.K. Hall, Oxidation–reduction properties of copper- and nickel-substituted hydroxyapatites, J. Phys. Chem. 77 (1973) 791–800.
[63] R.G. Herman, D.R. Flentge, Electron paramagnetic resonance parameters of copper(II) Y zeolites, J. Phys. Chem. 82 (1978) 720–729.
[64] J.R. Davis, A.I.H. Committee, Copper and Copper Alloys, ASM International, 2001.
[65] H. Bothe, D.J. Darley, S.P. Albracht, G.J. Gerfen, B.T. Golding, W. Buckel, Identification of the 4-glutamyl radical as an intermediate in the carbon skeleton rearrangement catalyzed by coenzyme B12-dependent glutamate mutase from *Clostridium cochlearium*, Biochemistry 37 (1998) 4105.
[66] V. Bandarian, G.H. Reed, Hydrazine cation radical in the active site of ethanolamine ammonia-lyase: mechanism-based inactivation by hydroxyethylhydrazine, Biochemistry 38 (1999) 12394–12402.
[67] G.J. Gerfen, EPR spectroscopy of B12-dependent enzymes, in: R. Banerjee (Ed.), Chemistry and Biochemistry of B12, Wiley, New York, 1999.
[68] A. Abend, V. Bandarian, G.H. Reed, P.A. Frey, Identification of cis-ethanesemidione as the organic radical derived from glycolaldehyde in the suicide inactivation of dioldehydrase and of ethanolamine ammonia-lyase, Biochemistry 39 (2000) 6250–6257.
[69] S.S. Eaton, G.R. Eaton, Distance measurements by SW and pulsed EPR, Distance Measurements in Biological Systems by EPR, first ed., Springer, 2001.
[70] V. Bandarian, G.H. Reed, Analysis of the electron paramagnetic resonance spectrum of a radical intermediate in the coenzyme B12-dependent ethanolamine ammonia-lyase catalyzed reaction of S-2-aminopropanol, Biochemistry 41 (2002) 8580–8588.
[71] S.C. Ke, Spin–spin interaction in ethanolamine deaminase, Biochim. Biophys. Acta – Gen. Subjects 1620 (2003) 267–272.
[72] S.O. Mansoorabadi, R. Padmakumar, N. Fazliddinova, M. Vlasie, R. Banerjee, G.H. Reed, Characterization of a succinyl-CoA radical-cob(II)alamin spin triplet intermediate in the reaction catalyzed by adenosylcobalamin-dependent methylmalonyl-CoA mutase, Biochemistry 44 (2005) 3153.
[73] S.O. Mansoorabadi, O.T. Magnusson, R.R. Poyner, P.A. Frey, G.H. Reed, Analysis of the Cob(II)alamin -5′-deoxy-3′,4′-anhydroadenosyl radical triplet spin system in the active site of diol dehydrase, Biochemistry 45 (2006) 14362–14370.
[74] S.O. Mansoorabadi, J. Seravalli, C. Furdui, V. Krymov, G.J. Gerfen, T.P. Begley, J. Melnick, S.W. Ragsdale, G.H. Reed, EPR spectroscopic and computational characterization of the hydroxyethylidene-thiamine pyrophosphate radical intermediate of pyruvate: ferredoxin oxidoreductase, Biochemistry 45 (2006) 7122–7131.
[75] J. Yoon, E.I. Solomon, Electronic structures of exchange coupled trigonal trimeric Cu(II) complexes: spin frustration, antisymmetric exchange, pseudo-A terms, and their relation to O2 activation in the multicopper oxidases, Coord. Chem. Rev. 251 (2007) 379–400.
[76] K. Tang, S.O. Mansoorabadi, G.H. Reed, P.A. Frey, Radical triplets and suicide inhibition in reactions of 4-thia-d- and 4-thia-L-lysine with lysine 5,6-aminomutase, Biochemistry 48 (2009) 8151–8160.
[77] R.C. Bray, Electron paramagnetic resonance in biochemistry, FEBS Lett. 5 (1969) 1–6.
[78] E. Antonini, M. Brunori, Hemoglobin and Myoglobin in their Reactions with Ligands, North-Holland Pub. Co., Amsterdam, 1971.
[79] A. Brancaccio, F. Cutruzzola, C. Allocatelli, M. Brunori, S. Smerdon, A. Wilkinson, Y. Dou, D. Keenan, M. Ikeda-Saito, R. Brantley, Structural factors governing azide and cyanide binding to mammalian metmyoglobins, J. Biol. Chem. 269 (1994) 13843–13853.
[80] J. Peisach, W.E. Blumberg, B.A. Wittenberg, J.B. Wittenberg, Configuration of the heme and its ligands, J. Biol. Chem. 243 (1968) 1871–1880.
[81] J. Peisach, W. Mims, J. Davis, Water coordination by heme iron in metmyoglobin, J. Biol. Chem. 259 (1984) 2704–2706.
[82] W.E. Blumberg, J. Peisach, The measurement of zero field splitting and the determination of ligand composition in mononuclear nonheme iron proteins, Ann. NY Acad. Sci. 222 (1973) 539–560.
[83] W. Blumberg, J. Peisach, Probes of Structure and Function of Macromolecules and Membranes, Academic Press, New York, 1971.
[84] A. Lévy, P. Kuppusamy, J.M. Rifkind, Multiple heme pocket subconformations of methemoglobin associated with distal histidine interactions, Biochemistry 29 (1990) 9311–9316.
[85] J. Lin, J. Merryweather, L.B. Vitello, J.E. Erman, Metmyoglobin/azide: the effect of heme-linked ionizations on the rate of complex formation, Arch. Biochem. Biophys. 362 (1999) 148–158.
[86] S. Oellerich, E. Bill, P. Hildebrandt, Freeze-quench resonance Raman and electron paramagnetic resonance spectroscopy for studying enzyme kinetics: application to azide binding to myoglobin, Appl. Spectrosc. 54 (2000) 1480–1484.
[87] J.A. Hamilton, Y. Tamao, R.L. Blakley, R.E. Coffman, Cobamides and ribonucleotide reduction. X. Electron paramagnetic resonance studies on cobalamin-dependent ribonucleotide reduction, Biochemistry 11 (1972) 4696–4705.
[88] J.A. Berson, Meta-quinonoid compounds, in: S. Patai, Z. Rappoport (Eds.), The Chemistry of Quinoid Compounds, Wiley, 1988.
[89] G. Spagnol, K. Shiraishi, S. Rajca, A. Rajca, Triplet ground state (S = 1) pegylated bis(aminoxyl) diradical: synthesis and the effect of water on magnetic properties, Chem. Commun. (2005) 5047–5049.
[90] C. Riplinger, J.P.Y. Kao, G.M. Rosen, V. Kathirvelu, G.R. Eaton, S.S. Eaton, A. Kutateladze, F. Neese, Interaction of radical pairs through-bond and through-space. Scope and limitations of the point-dipole approximation in electron paramagnetic resonance spectroscopy, J. Am. Chem. Soc. 131 (2009) 10092–10106.
[91] Y. Kurita, W. Gordy, Electron spin resonance in a gamma-irradiated single crystal of L-cystine dihydrochloride, J. Chem. Phys. 34 (1961) 282–288.
[92] H.C. Box, Free-radical formation by ultraviolet irradiation in single crystals of cysteine HCl, J. Chem. Phys. 45 (1966) 809.
[93] W.W.H. Kou, H.C. Box, Primary radiation products in cysteine hydrochloride, J. Chem. Phys. 64 (1976) 3060–3062.
[94] J.H. Hadley, W. Gordy, Nuclear coupling of 33S and the nature of free radicals in irradiated crystals of N-acetyl-L-cysteine, Proc. Natl. Acad. Sci. USA 74 (1977) 216–220.
[95] M. Engström, O. Vahtras, H. Ågren, Hydrogen bonding to tyrosyl radical analyzed by ab initio *g*-tensor calculations, Chem. Phys. Lett. 328 (2000) 483–491.
[96] M. van Gastel, J.W.A. Coremans, H. Sommerdijk, M.C. van Hemert, E.J.J. Groenen, An ab initio quantum chemical study of the blue-copper site of azurin, J. Am. Chem. Soc. 124 (2002) 2035.
[97] G. Lassmann, M. Kolberg, G. Bleifuss, A. Graslund, B. Sjöberg, W. Lubitz, Protein thiyl radicals in disordered systems: a comparative EPR study at low temperature, Phys. Chem. Chem. Phys. 5 (2003) 2442–2453.
[98] M. van Gastel, W. Lubitz, G. Lassmann, F. Neese, Electronic structure of the cysteine thiyl radical: a DFT and correlated ab initio study, J. Am. Chem. Soc. 126 (2004) 2237–2246.
[99] J.A. Weil, J.R. Bolton, J.E. Wertz, Electron Paramagnetic Resonance: Elementary Theory and Practical Applications, Wiley, New York, 1994.
[100] P. Atkins, J.D. Paula, Physical Chemistry, eight ed., W.H. Freeman, 2006.
[101] K. Matsuki, J.H. Hadley, W.H. Nelson, C.Y. Yang, E.S.R. Studies, ESR studies of monosulfide radicals in irradiated N-acetyl-L-cysteine single crystals, J. Magn. Reson. Ser. A 103 (1993) 196–202.

[102] D. Nelson, M.C.R. Symons, The detection of thiyl radicals by ESR spectroscopy, Chem. Phys. Lett. 36 (1975) 340–341.
[103] M. Kolberg, G. Bleifuss, A. Gräslund, B. Sjöberg, W. Lubitz, F. Lendzian, G. Lassmann, Protein thiyl radicals directly observed by EPR spectroscopy, Arch. Biochem. Biophys. 403 (2002) 141–144.
[104] M. Engstrom, F. Himo, A. Graslund, B. Minaev, O. Vahtras, H. Agren, Hydrogen bonding to tyrosyl radical analyzed by ab initio g-tensor calculations, J. Phys. Chem. A 104 (2000) 5149–5153.
[105] D.J. Nelson, R.L. Petersen, M.C.R. Symons, The detection of thiyl radicals by ESR spectroscopy, J. Chem. Soc., Perkin Trans. 2 (1977) 2005–2015.
[106] J.C. Wilson, G. Wu, A. Tsai, G.J. Gerfen, Determination of the structural environment of the tyrosyl radical in prostaglandin H2 synthase-1: a high frequency ENDOR/EPR study, J. Am. Chem. Soc. 127 (2005) 1618–1619.
[107] J. Retey, Enzymic reaction selectivity by negative catalysis or how do enzymes deal with highly reactive intermediates, Angew. Chem., Int. Edn. Engl. 29 (1990) 355.
[108] D.B. Goodin, D.E. McRee, The Asp-His-iron triad of cytochrome c peroxidase controls the reduction potential electronic structure, and coupling of the tryptophan free radical to the heme, Biochemistry 32 (1993) 3313–3324.
[109] C.W. Hoganson, N. Lydakis-Simantiris, X. Tang, C. Tommos, K. Warncke, G.T. Babcock, B.A. Diner, J. McCracken, S. Styring, A hydrogen-atom abstraction model for the function of YZ in photosynthetic oxygen evolution, Photosynth. Res. 46 (1995) 177–184.
[110] C.W. Hoganson, M. Sahlin, B. Sjöberg, G.T. Babcock, Electron magnetic resonance of the tyrosyl radical in ribonucleotide reductase from *Escherichia coli*, J. Am. Chem. Soc. 118 (1996) 4672–4679.
[111] G.T. Babcock, M. Espe, C. Hoganson, N. Lydakis-Simantiris, J. McCracken, W. Shi, S. Styring, C. Tommos, K. Warncke, Tyrosyl radicals in enzyme catalysis: some properties and a focus on photosynthetic water oxidation, Acta Chem. Scand. 51 (1997) 533–540.
[112] M.D. Vlasie, R. Banerjee, Tyrosine 89 accelerates co-carbon bond homolysis in methylmalonyl-CoA mutase, J. Am. Chem. Soc. 125 (2003) 5431–5435.
[113] C.E. Rogge, B. Ho, W. Liu, R.J. Kulmacz, A. Tsai, Role of Tyr348 in Tyr385 radical dynamics and cyclooxygenase inhibitor interactions in prostaglandin H synthase-2, Biochemistry 45 (2006) 523–532.
[114] C. Tsai, A. del Sol, R. Nussinov, Protein allostery, signal transmission and dynamics: a classification scheme of allosteric mechanisms, Mol. Biosyst. 5 (2009) 207.
[115] S. Shan, D. Herschlag, The change in hydrogen bond strength accompanying charge rearrangement: implications for enzymatic catalysis, Proc. Natl. Acad. Sci. USA 93 (1996) 14474–14479.
[116] J.A. Gerlt, Stabilization of reactive intermediates and transition states in enzyme active sites by hydrogen bonding, in: Comprehensive Natural Products Chemistry, Pergamon, Oxford, 1999, pp. 5–29.
[117] H. Guo, D.R. Salahub, Cooperative hydrogen bonding and enzyme catalysis, Angew. Chem., Int. Edit. 37 (1998) 2985–2990.
[118] C.N. Fuhrmann, B.A. Kelch, N. Ota, D.A. Agard, J. Mol. Biol. 338 (2004) 999–1013.
[119] C.N. Fuhrmann, M.D. Daugherty, D.A. Agard, The 0.83 Å resolution crystal structure of [alpha]-lytic protease reveals the detailed structure of the active site and identifies a source of conformational strain, J. Am. Chem. Soc. 128 (2006) 9086–9102.
[120] P.W. Anderson, Antiferromagnetism. Theory of superexchange interaction, Phys. Rev. 79 (1950) 350.
[121] G. Buettner, R. Coffman, E. PR, EPR determination of the Co(II)-free radical magnetic geometry of the "doubleT" species arising in a coenzyme B-12-enzyme reaction, Biochim. Biophys. Acta – Enzymol. 480 (1977) 495–505.
[122] R.E. Coffman, G.R. Buettner, A limit function for long-range ferromagnetic and antiferromagnetic superexchange, J. Phys. Chem. 83 (1979) 2387–2392.
[123] O. Kahn, Dinuclear complexes with predictable magnetic properties, Angew. Chem., Int. Ed. Engl. 24 (1985) 834–850.
[124] G.H. Reed, S.O. Mansoorabadi, The positions of radical intermediates in the active sites of adenosylcobalamin-dependent enzymes, Curr. Opin. Struct. Biol. 13 (2003) 716–721.
[125] D.J. Hirsh, W.F. Beck, J.B. Lynch, L. Que, G.W. Brudvig, Using saturation-recovery EPR to measure exchange couplings in proteins: application to ribonucleotide reductase, J. Am. Chem. Soc. 114 (1992) 7475–7481.
[126] P.F. Richardson, R.W. Kreilick, Transition metal complexes with radical ligands: pyridyliminonitroxide radicals with copper and vanadium, J. Magn. Reson. 29 (1978) 285–291.
[127] P.F. Richardson, R.W. Kreilick, Complexes of free radicals with transition metals. Manganese bis(hexafluoroacetylacetonate) and vanadyl bis(trifluoroacetylacetonate) with pyridylimino nitroxide and pyridylnitronyl nitroxide radicals, J. Phys. Chem. 82 (1978) 1149–1151.
[128] J. Pilbrow, Transition Ion Electron Paramagnetic Resonance, Clarendon Press, 1990.
[129] D.A. Dougherty, Spin control in organic molecules, Acc. Chem. Res. 24 (1991) 88–94.
[130] P. Hofmann, Solid State Physics: An Introduction, Solid State Physics: An Introduction, Wiley-VCH, 2008.
[131] P.K. Sharma, Z.T. Chu, M.H.M. Olsson, A. Warshel, A new paradigm for electrostatic catalysis of radical reactions in vitamin B12 enzymes, Proc. Natl. Acad. Sci. 104 (2007) 9661–9666.
[132] P.A. Sigala, M.A. Tsuchida, D. Herschlag, Hydrogen bond dynamics in the active site of photoactive yellow protein, Proc. Natl. Acad. Sci. 106 (2009) 9232–9237.
[133] S. Yamaguchi, H. Kamikubo, K. Kurihara, R. Kuroki, N. Niimura, N. Shimizu, Y. Yamazaki, M. Kataoka, Low-barrier hydrogen bond in photoactive yellow protein, Proc. Natl. Acad. Sci. 106 (2009) 440–444.
[134] G.L. Holliday, J.B. Mitchell, J.M. Thornton, Understanding the functional roles of amino acid residues in enzyme catalysis, J. Mol. Biol. 390 (2009) 560–577.
[135] J.P. Klinman, An integrated model for enzyme catalysis emerges from studies of hydrogen tunneling, Chem. Phys. Lett. 471 (2009) 179–193.
[136] D.A. Kraut, P.A. Sigala, T.D. Fenn, D. Herschlag, Dissecting the paradoxical effects of hydrogen bond mutations in the ketosteroid isomerase oxyanion hole, Proc. Natl. Acad. Sci. 107 (2010) 1960–1965.
[137] P.M. Kozlowski, T. Kamachi, M. Kumar, T. Nakayama, K. Yoshizawa, Theoretical analysis of the diradical nature of adenosylcobalamin cofactor-tyrosine complex in B12-dependent mutases: inspiring PCET-driven enzymatic catalysis, J. Phys. Chem. B 114 (2010) 5928–5939.
[138] A. Warshel, P.K. Sharma, M. Kato, Y. Xiang, H. Liu, M.H.M. Olsson, Electrostatic basis for enzyme catalysis, electrostatic basis for enzyme catalysis, Chem. Rev. 106 (2006) 3210–3235.
[139] X. Li, L.W. Chung, P. Paneth, K. Morokuma, DFT and ONIOM(DFT:MM) studies on Co–C bond cleavage and hydrogen transfer in B12-dependent methylmalonyl-CoA mutase. Stepwise or concerted mechanism?, J Am. Chem. Soc 131 (2009) 5115–5125.
[140] K. Gruber, R. Reitzer, C. Kratky, Radical shuttling in a protein: ribose pseudorotation controls alkyl-radical transfer in the coenzyme B12 dependent enzyme glutamate mutase, Angew. Chem., Int. Ed. 40 (2001) 3377–3380.
[141] N. Dölker, F. Maseras, P.E.M. Siegbahn, Stabilization of the adenosyl radical in coenzyme B12 – a theoretical study, Chem. Phys. Lett. 386 (2004) 174–178.
[142] N. Dölker, A. Morreale, F. Maseras, Computational study on the difference between the Co–C bond dissociation energy in methylcobalamin and adenosylcobalamin, J. Biol. Inorg. Chem. 10 (2005) 509–517.
[143] K.P. Jensen, U. Ryde, How the Co–C bond is cleaved in coenzyme B12 enzymes: a theoretical study, J. Am. Chem. Soc. 127 (2005) 9117–9128.
[144] W. Buckel, Highlight: radicals in enzymatic catalysis, Biol. Chem. 386 (2005) 949.
[145] K.P. Jensen, U. Ryde, How the Co–C bond is cleaved in coenzyme B12 enzymes: a theoretical study, Coord. Chem. Rev. 253 (2009) 769–778.
[146] B. Durbeej, G. Sandala, D. Bucher, D. Smith, L. Radom, On the importance of ribose orientation in the substrate activation of the coenzyme B12-dependent mutases, Chem. Eur. J. 15 (2009) 8578–8585.
[147] A.R. Jones, J.R. Woodward, N.S. Scrutton, A new conceptual framework for enzyme catalysis, J. Am. Chem. Soc. 131 (2009) 17246–17253.
[148] P.F. Richardson, R.W. Kreilick, Copper complexes with free-radical ligands, J. Am. Chem. Soc. 99 (1977) 8183–8187.
[149] G. Dismukes, H.A. Frank, R. Friesner, K. Sauer, Electronic interactions between iron and the bound semiquinones in bacterial photosynthesis. EPR spectroscopy of oriented cells of *Rhodopseudomonas viridis*, Biochim. Biophys. Acta – Bioenerg. 764 (1984) 253–271.
[150] K.M. More, G.R. Eaton, S.S. Eaton, Metal-nitroxyl interactions. 47. EPR spectra of two-spin-labeled derivatives of EDTA coordinated to paramagnetic metal ions, Inorg. Chem. 25 (1986) 2638–2646.
[151] L. Fielding, K.M. More, G.R. Eaton, S.S. Eaton, Metal-nitroxyl interactions. 46. EPR spectra of low-spin iron(III) complexes of spin-labeled tetraphenylporphyrins and their implications for the interpretation of EPR spectra of spin-labeled cytochrome P450, J. Am. Chem. Soc. 108 (1986) 618–625.
[152] L. Fielding, K.M. More, G.R. Eaton, S.S. Eaton, Metal-nitroxyl interactions. 51. Collapse of iron-nitroxyl electron–electron spin–spin splitting due to the increase in the electron spin relaxation rate for high-spin iron(III) when temperature is increased, J. Am. Chem. Soc. 108 (1986) 8194–8196.
[153] G. Bender, R.R. Poyner, G.H. Reed, Identification of the substrate radical intermediate derived from ethanolamine during catalysis by ethanolamine ammonia-lyase, Biochemistry 47 (2008) 11360–11366.
[154] D.E. Goldsack, W.S. Eberlein, R.A. Alberty, Effect of heme-linked groups on ligand binding, J. Biol. Chem. 241 (1966) 2653–2660.
[155] J. Suarez, K. Ranguelova, A.A. Jarzecki, J. Manzerova, V. Krymov, X. Zhao, S. Yu, L. Metlitsky, G.J. Gerfen, R.S. Magliozzo, An oxyferrous heme/protein-based radical intermediate is catalytically competent in the catalase reaction of *M. tuberculosis* catalase-peroxidase (KatG), J. Biol. Chem. 284 (2009) 7017–7029.
[156] A. Bencini, EPR of Exchange Coupled Systems, Springer-Verlag, Berlin, 1990.
[157] S.G. Eaton, G.R. Eaton, Measurement of spin–spin distances from the intensity of the EPR half-field transition, J. Am. Chem. Soc. 104 (1982) 5002–5003.
[158] S.G. Eaton, K.M. More, B.M. Sawant, G.R. Eaton, Use of the ESR half-field transition to determine the interspin distance and the orientation of the interspin vector in systems with two unpaired electrons, J. Am. Chem. Soc. 105 (1983) 6560–6567.
[159] J. Svorec, M. Valko, J. Moncol, M. Mazúr, M. Melník, J. Telser, Determination of intermolecular copper–copper distances from the EPR half-field transitions and their comparison with distances from X-ray structures: applications to copper(II) complexes with biologically important ligands, Transition. Met. Chem. 34 (2009) 129–134.
[160] D.A. Shultz, C. P Mussari, K.K. Ramanathan, J.W. Kampf, Electron spin–spin exchange coupling mediated by the porphyrin-system, Inorg. Chem. 45 (2006) 5752–5759.